biomolecules

MDPI

Article

Cyclo-(His-Phe) Complexes with Copper and Zinc Nanoparticles Have Antimicrobial Properties and Targeted Anticancer Potential Against Osteosarcoma Cells

Chrysanthi Pinelopi Apostolidou [1,2], Georgios Charalambidis [3,4], Aikaterini Gialouri [1,5], Maria Chatzinikolaidou [1,2] and Anna Mitraki [1,2,*]

[1] Department of Materials Science and Engineering, University of Crete, Voutes Campus, 70013 Heraklion, Greece; chrysana@materials.uoc.gr (C.P.A.); med12p1170068@med.uoc.gr (A.G.); mchatzin@uoc.gr (M.C.)
[2] Institute of Electronic Structure and Laser (IESL), Foundation for Research and Technology-Hellas (FORTH), 70013 Heraklion, Greece
[3] Laboratory of Bioinorganic Chemistry, Department of Chemistry, University of Crete, Voutes Campus, 70013 Heraklion, Greece; gcharal@eie.gr
[4] Theoretical and Physical Chemistry Institute, National Hellenic Research Foundation, 48 Vassileos Constantinou Ave., 11635 Athens, Greece
[5] School of Medicine, University of Crete, 70013 Heraklion, Greece
* Correspondence: mitraki@materials.uoc.gr or mitrakia@uoc.gr

Abstract

Copper and zinc nanoparticles have been suggested as potent anticancer agents, particularly against osteosarcoma, a highly aggressive bone cancer with limited treatment options. In order to avoid systemic toxicity, biomolecular carriers able to chelate metal ions and deliver them in a targeted manner to the vicinity of cancer cells need to be developed. Herein, we have used a histidine-containing, cyclic dipeptide as a carrier able to chelate stabilized copper and zinc nanoparticles. The cyclic peptide cyclo-(histidine-phenylalanine) (cHF) self-assembled into amyloid-type fibrils; morphological and structural characterization following metal addition confirmed the formation of cHF−CuNPs and cHF–ZnNPs. These composite nanoparticles demonstrated bacteriostatic activity against *Escherichia coli* and *Staphylococcus aureus* at the in vitro level. We evaluated the optimal concentration of cHF–metalNP complexes with limited cytotoxicity to L929 fibroblasts and high cytotoxic effects against MG-63 osteosarcoma cells. Their cytotoxicity was particularly pronounced at pH 6.4, which emulates the tumor microenvironment. The cHF peptide alone did not demonstrate significant antimicrobial or cytotoxic effects to both cell types, suggesting that it can act as a cytocompatible, pH-responsive carrier of metal ions with targeted dual functionality against both microbial infections and osteosarcoma cancer cells.

Keywords: self-assembling peptides; amyloid fibrils; metal nanoparticles; antimicrobial activity; fibroblasts; osteosarcoma

Academic Editor: Francesco Scaglione

Received: 18 December 2025
Revised: 28 January 2026
Accepted: 8 February 2026
Published: 11 February 2026

1. Introduction

The development of chemotherapy agents that exploit molecular platforms for targeted delivery in cancer cells is a crucial area in modern molecular medicine [1]. The purpose of targeted delivery is to develop carriers that could locally and specifically release therapeutic cargo in the tumor microenvironment (TME) of cancer cells, in this way minimizing the exposure of normal cells and avoiding the inducement of systemic toxicity. Osteosarcoma

(OS) is a highly aggressive bone cancer with limited treatment options [2]. OS is the most common bone malignancy, particularly prevalent in children and adolescents. It is typically treated with surgical resection of the tumor tissue, followed by long-term chemotherapy to prevent recurrence [3]. The tumor microenvironment is characterized by an acidic pH, elevated levels of glutathione (GSH), and hydrogen peroxide (H_2O_2) [4]. In osteosarcoma, metabolic adaptation, increased aggressiveness and increased resistance to chemotherapy drugs have been attributed to the acid TME [5,6]. Osteosarcoma-targeted nanoparticles for conventional chemotherapy drugs such as polymeric nanoparticles, gold nanoparticles, and liposomes have been reported [7].

Inorganic nanomaterials have been proposed for alternative novel treatments against osteosarcoma [8]. Recent research has also suggested the potential of copper and zinc complexes as therapeutic agents against osteosarcoma cells [9]. In small amounts [10], metal ions such as iron, zinc, copper, and magnesium are essential elements that play critical roles in various biochemical processes, including enzyme function, oxygen transport, and cellular signaling [11]. In eukaryotic organisms, both zinc and copper are involved in innate immune defense mechanisms, where controlled metal ion fluxes and localized oxidative stress contribute to the elimination of invading pathogens [12]. However, at concentrations above 1 mM, both copper and zinc substantially decrease the viability of model cell lines such as fibroblasts [13] and can lead to toxicity and adverse health effects [14].

Upon exposure to biological or aqueous solutions, metallic nanoparticles can release free metal ions and generate reactive oxygen species (ROS). Excessive ROS production, including hydrogen peroxide (H_2O_2), superoxide anions ($O_2^{\bullet-}$), and hydroxyl radicals ($HO^{\bullet}$), disrupts cellular redox homeostasis and can damage essential biomolecules [15].

To avoid the toxicity and aggregation issues associated with "naked" metal nanoparticles, and achieve targeted delivery and maximal efficiency, metal ions need to be combined with biomaterials, such as polymers, liposomes, hydrogels, etc. [16]. Metal ion-chelating biological molecules are promising for nanoparticle synthesis and stabilization due to their biocompatibility and the diverse range of physicochemical advantages they confer [17]. Especially, the acid TME can be exploited for targeted delivery by metal-chelating molecules that can release their metal ion cargo in acid pH and avoid systemic toxicity to healthy cells. Amongst these biomolecules, peptides confer versatile chemical functionalities for metal coordination [18], facilitating the conjugation and integration of a wide range of therapeutic cargoes into the peptide matrix and therefore making them attractive candidates for applications in theragnostic and drug delivery applications [19]. In particular, the imidazole group in the side chain of histidine can directly interact with and bind to metal ions and renders histidine a key modulator in biological assembly processes [20]. This role can be emulated through the introduction of a histidine residue in designer peptide materials targeted for a variety of applications in bio-nanotechnology and biomedicine [21]. Histidine can serve as a capping or chelating agent, conveying stability to the formed nanoparticles. Most importantly, it conveys a pH-responsive behavior due to the protonation of the imidazole ring of histidine under acidic conditions, making it an attractive candidate for forming a pH-sensitive drug delivery system [22]. This pH-responsive behavior presents a unique therapeutic challenge and opportunity since the tumor microenvironment is characterized by an acidic pH and elevated levels of glutathione (GSH) and hydrogen peroxide (H_2O_2) [4]. NPs containing histidine respond dynamically to these pH fluctuations. The acidic tumor microenvironment prompts the protonation of pH-sensitive moieties in the NPs. These changes disrupt the hydrophilic–hydrophobic balance of the histidine–NP complexes, leading to the release of therapeutic cargo [22]. Histidine-containing peptides can also co-assemble with metal ions and photosensitizers, forming carriers for intracellular imaging [23] or metallo-nanodrugs for photodynamic therapy [24]. Amongst peptide carri-

ers, cyclic dipeptides are particularly promising self-assembling scaffolds with a plethora of bioactive activities, such as antimicrobial [25], antitumor, and antiviral activities [26]. Recent computational and experimental research revealed the potential of the cyclo-L-histidine-D-histidine (Cyclo-$_L$H$_D$H) peptide to co-assemble with anticancer drugs into spherical nanostructures and successfully deliver them into HeLa cells [27,28] and further extended the concept to histidine-containing tetrapeptides [29].

Herein, we focused on studying the self-assembly propensity of a phenylalanine- and histidine-containing cyclic peptide, specifically cyclic-(His-Phe), hereinafter referred to as (cHF) (Scheme 1). The antitumor activity of (cHF) itself has been previously reported; however, its effects on osteosarcoma cells have not been investigated [30]. Its eventual self-assembling properties have not been evaluated. We anticipated that the peptide would self-assemble, due to the strong hydrogen bonding propensity of the peptide ring carbonyl and amino moieties and the presence of the phenylalanine ring known to promote self-assembly via π-π* aromatic interactions. We further investigated the ability of the peptide for in situ synthesis of copper (cHF–CuNPs) and zinc nanoparticles (cHF–ZnNPs) upon reduction. We carried out their morphological and physicochemical characterization with FESEM, TEM and FTIR and their biological characterization with in vitro antimicrobial assays, the effect on fibroblasts and osteosarcoma cell lines, and reactive oxygen species evaluation. We evaluated the optimal concentration of nanoparticles with limited cytotoxicity to a L929 fibroblast cell line and high cytotoxic effects against MG-63 osteosarcoma cells, especially at pH 6,4 that emulates the TME. We further tested their effect on *Escherichia coli* (*E. coli*) and *Staphylococcus aureus* (*S. aureus*) bacterial cells, since antimicrobial properties are very important in order to avoid infections in post-surgery sites and post-chemotherapy treatments. The cHF peptide alone did not demonstrate significant antimicrobial or cytotoxic effects to both cell types. By harnessing the synergistic effects of pH-responsive peptide scaffolds as carriers of metal nanoparticle cargoes, we sought to develop a cytocompatible, responsive material with targeted dual functionality against both microbial infections and osteosarcoma cancer cells.

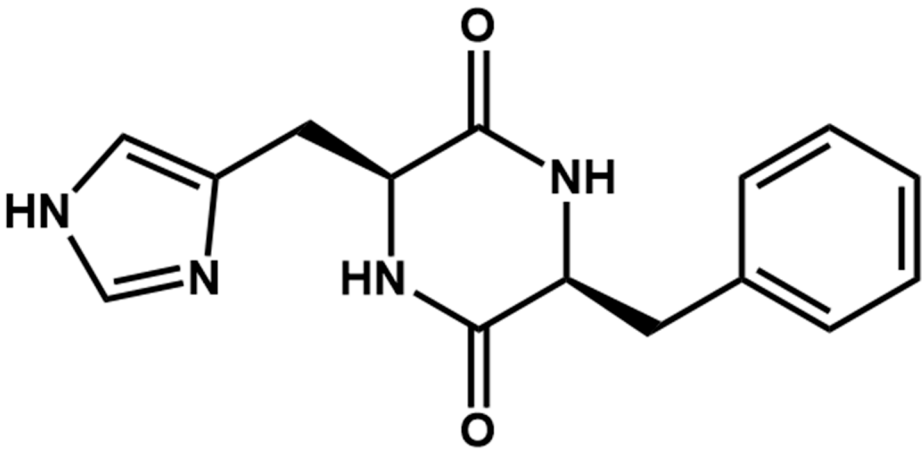

Scheme 1. Chemical structure of the dipeptide cyclo-(His-Phe).

2. Materials and Methods

2.1. Materials

Cyclo-(His-Phe) (cHF) peptide powder was purchased by Bachem product number 4006752, (Bubendorf, Switzerland). The purity of the peptide was higher than 95%. The fibroblasts L929 and osteosarcoma MG-63 cell lines were cultured at 37 °C, 5% CO_2 in DMEM (Gibco) supplemented with 10% fetal bovine serum (Gibco, Thermo Fisher Scientific, Waltham, MA, USA) and 50 μg/mL gentamycin (Applichem, Darmstadt, Germany).

Sodium borohydride ($NaBH_4$), phosphate-buffered saline (PBS), Thiazolyl blue tetrazolium bromide (MTT), and Congo Red were purchased from Sigma-Aldrich (St. Louis, MO, USA).

2.2. Sample Preparation

Initially, 1.3 mg of cHF peptide powder was weighed and dissolved in 1 mL PBS under heating at 40 °C and sonication for 20 min. When the samples became transparent, indicating the complete dissolution of the peptide powder, a sample was taken for FESEM examination and subsequently the appropriate amount of zinc or copper chloride from 0.1 M stock solutions was added to obtain four different molar peptide-to-metal ratios. The ratios used ranged from 1:1 molar ratio of peptide to metal salts (5 mM peptide to 5 mM metal salt) to 10:1 molar ratio peptide to metal salt (5 mM peptide to 0.5 mM metal salts) corresponding to final metal ion concentrations of 0.5, 1, 2.5, and 5 mM, respectively, based on the initial peptide concentration and dilution from 0.1 M metal stock solutions. The final volume of each sample was adjusted to 1 mL. The samples were incubated for 70 min at ambient temperature and centrifuged at 7000 rpm for 10 min. Then, the supernatant was removed and the pellet re-dispersed in 1 mL of water. Freshly prepared reducing agent $NaBH_4$ (0.25 M) was added in a molar ratio of metal to a reducing agent of 1 to 1. The samples were incubated for 45 min at 80 °C and then at room temperature overnight. The next day, the samples were centrifuged at 7000 rpm for 15 min, the supernatant was discarded, and the pellet was re-dispersed in 1 mL of water. This step was repeated twice. In the last step, the reduced peptide–ion complexes were redissolved in 1 mL of pure ethanol. After centrifugation, the pellet was left at 80 °C to dry and stored in the refrigerator. Before each experiment, the samples were re-dispersed in PBS, to achieve a final peptide concentration of 5 mM, and sonicated in a bath at ambient temperature for 5 min. Finally, the samples were exposed to ultraviolet light for 15 min before exposure to cell cultures to avoid bacterial contamination.

2.3. Morphological Characterization of cHF Self-Assembly and Its Complexes with CuNPs and ZnNPs

2.3.1. Field-Emission Scanning Electron Microscopy (FESEM) and Energy-Dispersive X-Ray Spectroscopy (EDX) Analysis

A volume of 10 μL of each peptide sample was deposited on a glass cover and air-dried overnight. Dried samples were covered with 10 nm of Au sputtering (Baltec SCD 050, Bal-Tec AG, Pfäffikon, Switzerland). Observation experiments were performed using a JEOL JSM-7000F microscope (Akishima, Tokyo, Japan) operating at 15 kV and the composition determined by EDX using an Oxford Link ISIS System (Oxford, UK). The analysis was carried out by determining the intensity of a characteristic X-ray peak of a chosen element on a standard that has no interfering peaks.

2.3.2. Transmission Electron Microscopy (TEM) Analysis

A volume of 8 μL of the 0.5 mM aqueous PBS solution containing the sample (dilution 1:10) was deposited for 90 s on the shiny side of the carbon-formvar grid. The excess fluid was removed with the edge of an absorptive paper. Then, 8 μL of uranyl acetate (1%) was added. The samples were ready for further investigation under JEOL JEM-2100 TEM (Akishima, Tokyo, Japan) at 200 kV.

2.3.3. Congo Red Staining

Each peptide solution (20 μL) was thoroughly mixed with 5 μL of a fresh Congo Red assay solution (10 mM Congo Red, 2.5 mM NaOH in 50% ethanol). A drop of the mixture was deposited onto a glass coverslip and was examined before or after drying at room

temperature, with a Zeiss Stemi 2000-C microscope (Oberkochen, Germany) with and without the use of a crossed polarizer.

2.3.4. Attenuated Total Reflectance Fourier-Transform Infrared Spectroscopy (ATR-FTIR) Analysis

Infrared spectra of the pristine cyclo-(His-Phe) and its complexes with Cu and Zn (cHF–CuNPs and cHF–ZnNPs) were collected in dried samples in order to analyze the chemical structure of these compounds. The ATR-FTIR spectra were collected in the wavenumber range of 400–4000 cm^{-1}. Spectra were collected with 4 cm^{-1} resolution and 128 scans. Attenuated total reflectance Fourier-transform infrared spectroscopy (ATR-FTIR) measurements were performed with a NICOLET 6700 FT-IR spectrometer (Waltham, MA, USA).

2.3.5. pH Responsiveness of the cHF–CuNPs and cHF–ZnNPs

The pH responsiveness of the cHF–CuNPs and cHF–ZnNPs was evaluated by preparing the samples in PBS at physiological conditions (pH 7.4); subsequently, the samples were collected, washed and dried as previously described. They were then resuspended at mildly acidic conditions (pH 6.4) for 24 h. They were further observed using FESEM and evaluated for their effect on osteosarcoma cells.

2.4. Biological Effect of cHF, cHF–CuNPs and cHF–ZnNPs

2.4.1. Cell Culture Maintenance

The human osteosarcoma MG-63 cells (American Type Culture Collection, CRL-1427) and L929 fibroblasts (ACC 2, DSMZ, Braunschweig, Germany) were cultured in DMEM with 10% fetal bovine serum and 50 µg/mL gentamycin. Cells were sustained in an incubator under a humidified atmosphere with 5% CO_2 at 37 °C.

2.4.2. Cytotoxicity Assessment on Fibroblasts and Osteosarcoma Cells by MTT

Cytotoxicity of the cHF peptide, cHF–CuNPs (0.5, 1, 2.5, and 5 mM) and cHF–ZnNPs (0.5, 1, 2.5, and 5 mM), as well as the metal ions of the salts $CuCl_2$ and $ZnCl_2$ at the corresponding concentrations, were assessed on L929 fibroblasts and MG-63 osteosarcoma cells by the MTT protocol. The L929 and MG-63 cell lines (1×10^4 cells/well) were cultured on 96-well plates.

Cells were incubated for 24 h or 48 h at 7.4 at 37 °C in 5% CO_2. For the pH 6.4 condition, the cells were seeded in pH 7.4 for 24 h and then cultured in pH 6.4 for the respective time of treatment (4, 24 and 48 h), according to the protocol used in osteosarcoma research [31].

Subsequently, the medium was removed, and the cHF–CuNPs and cHF–ZnNPs complexes were added in a total volume of 100 µL of culture medium. Untreated cells were used as controls. Following an incubation period of 24 h, the medium was carefully removed and replaced with 100 µL of fresh medium and 10 µL of MTT (5 mg/mL in PBS). The cells were incubated for 4 h to allow the development of the purple formazan products and the MTT/culture medium was substituted with 100 µL of an isopropanol–DMSO 1:1 solution. The formazan crystals were allowed to dissolve for 15 min at 37 °C. The absorbance was measured at 570 nm in a Synergy HTX BioTEK Plate Reader (Winooski, VT, USA). The tests were carried out in triplicate for each sample.

2.4.3. Bacterial Cell Viability

To evaluate the antibacterial effect of the synthesized samples, cHF–CuNPs (0.5, 1, 2.5, and 5 mM) and cHF–ZnNPs (0.5, 1, 2.5, and 5 mM), as well as $CuCl_2$ and $ZnCl_2$ at the corresponding concentrations, were tested against Gram-negative *E. coli* and Gram-positive *S. aureus* bacteria. Antibacterial efficacy was assessed by colony forming units

per mL (CFU/mL). All bacterial strains were maintained as glycerol stocks at −80 °C. The bacterial strains used in this study were kindly provided by the Department of Clinical Microbiology and Microbial Pathogenesis of the University Hospital in Heraklion, Greece, as previously described [32]. The bacterial strains of *E. coli* and *S. aureus* were inoculated and cultivated in Luria broth (LB) and incubated at 37 °C for 18–20 h at 200 rpm. Then, 500 μL of the pre-culture was transferred into 50 mL of LB and incubated in a shaker (200 rpm) at 37 °C until the mid-log phase (OD_{600} = 0.1) using a UV-Vis spectrophotometer (UV-1700 PharmaSpec; Shimazdu Corporation, Kyoto, Japan). The bacterial cells were diluted in the broth and 90 μL were subsequently added to wells of a 96-well plate to a final concentration of 10^5 CFU/mL. Each sample was redissolved in 100 μL PBS and 10 μL was then added to each well containing the bacteria suspension. The plates were incubated overnight at 37 °C and 10 μL of each well was subsequently serially diluted and plated in Luria broth agar plates. Following overnight incubation at 37 °C, colonies were counted. The results are presented as mean of triplicates of three independent experiments (n = 9).

2.4.4. Preparation of MG-63 Cells for Morphological Observation Under FESEM

MG-63 osteosarcoma cells were seeded on top of a circular cover glass of 10 mm inside a 24-well plate for 24 h. The next day, the cell medium was removed, and 100 μL of the cHF and its complexes were added on top. The plates were incubated at 37 °C for 24 h. After 24 h the medium where the complexes were diluted was removed and the attached cells were washed twice with 300 μL of sodium cacodylate (SCB) 0.1 M. The cells were stabilized with 4% paraformaldehyde for 30 min, washed with SCB 0.1 M and then followed by dehydration following successive 5 min incubations with graded concentrations of ethanol (30%, 50%, 70%, 90%, and 100% dry ethanol). Finally, 300 μL of hexamethyldisilazane were added to each well and left to evaporate overnight. The dehydrated samples were subjected to further processing for FESEM examination.

2.4.5. Intracellular ROS Measurements

Intracellular ROS production was evaluated using the fluorescent probe, 2′,7′-dichlorodihydrofluorescein diacetate (DCFDA, Sigma-Aldrich). MG-63 cells were seeded at a density of 1×10^4 per well in 96-well plates and incubated overnight at 37 °C in 5% CO_2. The cells were treated with cHF, cHF–CuNPs, and cHF_ZnNPs (1 mM) for 4 h and 24 h under physiological (pH 7.4) and mildly acidic conditions (pH 6.4). The following day, the cells were washed twice with PBS, and then were incubated with a solution of DCFDA in DMEM (10 μM, FBS-free) at 37 °C for 30 min. Ascorbic acid (AA) (1 mM) and H_2O_2 (200 μM) were used as negative and positive controls, respectively, and the treatment duration of cells with them was limited to 2 h prior to determination of cell viability by the MTT assay, in order to avoid long-term cell exposure to drastic conditions. The fluorescence intensity was measured by a BioTek microplate reader at an excitation filter of 485 nm and an emission filter of 528 nm. The fluorescence values were normalized to cell viability by dividing through the corresponding absorbance values from the MTT assay, in order to allow the production of ROS in treated cells to be compared with that in untreated samples.

$$\text{ROS normalized to cell viability}(\%) = \frac{(\text{Fsample} - \text{Fblank})/(\text{MTTsample} - \text{MTTblank})}{(\text{Fcontrol} - \text{Fblank})/(\text{MTTcontrol} - \text{MTTblank})} \times 100,$$

where F denotes DCF fluorescence and "control" denotes untreated cells. Untreated cells were set to be 100% intracellular ROS level for the normalization of the fluorescence intensity. For control experiments, cells were treated with ascorbic acid and hydrogen peroxide 2 h before ROS quantification. Experiments have been performed in quadruplicates.

2.4.6. Rescue Experiment by Treatment with Ascorbic Acid (AA)

A rescue experiment was performed to explore the possible recovery of reduced cell viability mediated by ROS via the effect of the metal ions. Based on previous reports [33], ascorbic acid was selected as a radical scavenger that protects against membrane oxidation and inhibits intracellular oxidative stress induced by nanoparticles. It may reverse the oxidative stress and thus the reduction in cell viability.

MG-63 cells were treated with 5 mM cHF, cHF–CuNPs (1 mM), cHF–ZnNPs (1 mM), 200 µM hydrogen peroxide, and 1 mM ascorbic acid for 4 h at pH 7.4 and 6.4. After 4 h, the treatment substances were removed, the cells were washed with PBS, and cell viability was measured by means of the MTT assay. In another plate, following removal of the treatment substances, 100 µL 0.5 mM ascorbic acid were added to each well, and incubated at 37 °C for 1 h. The AA was then removed, and fresh complete medium was added to the wells, followed by incubation for 24 h. After this time, cell viability was assessed by an MTT assay. Cell viability ratios were calculated by dividing the cell viability values of the samples treated with AA by the cell viability values of the samples without AA treatment. Samples were analyzed as mean ± standard deviation of quadruplicates.

2.5. Statistical Analysis

Statistical analysis was performed using ANOVA test in the GraphPad Prism version 8.3 to evaluate the significance of the differences between untreated cells and treatments with cHF–metal complexes at 24 h (designated using the symbol *) and 48 h (designated using the symbol †). These comparisons were carried out using one-way ANOVA with Welch's correction to ensure that the large sample sizes between experimental groups were more precisely analyzed followed by Dunnett T3 multiple-comparison tests. In experiments of the same sample size, one-way ANOVA followed by Dunnett multiple-comparison test has been performed. Comparisons between cHF–metal complexes and the corresponding metal salts (designated using the symbol #), as well as comparisons between cHF complexes under different pH conditions or different time points (designated using the symbol §), were performed using two-way ANOVA, followed by Sidak multiple-comparison tests. Data are expressed as means ± standard deviation (SD). Statistical significance was defined as (*, #, § or †) $p < 0.05$; ** or ## $p < 0.01$; *** or ### $p < 0.001$; **** or #### or §§§§ $p < 0.0001$; ns indicates a non-significant difference. The symbols *, #, §, and † denote different statistical comparisons and should not be interpreted as equivalent tests.

3. Results

3.1. Morphological Characterization of cHF, cHF–CuNPs and cHF–ZnNPs with FESEM and TEM

The samples taken following the dissolution of the peptide powder in PBS were examined with FESEM and TEM. Both techniques revealed the propensity of the cHF peptide to self-assemble into fibrillar structures (Figure 1A,B). Congo Red staining confirmed the amyloid-like nature of these fibrils, indicated by the characteristic green birefringence under a crossed polarizer (Figure 1C,D).

We subsequently studied the effect of adding copper ions ranging from 0.5 to 5 mM copper chloride. Following the addition of 0.5 mM $CuCl_2$, the fibrils displayed reduced thickness and increased condensation. Following treatment with $NaBH_4$, spherical structures in the range of 10 µm in diameter were formed, composed of multiple sub-segments (Figure S1). Increasing the $CuCl_2$ concentration to 1 mM promoted the formation of spherical "flower-like" structures with diameters in the range of 5 µm comprising nanosheets giving the appearance of petals (Figure 2A,B). Upon reduction, a similar morphology was observed, with the arrangement of nanosheets appearing denser and curved (Figure 2C,D). These morphological transformations suggest coordination between $CuCl_2$ and cHF pep-

tides, which promote rearrangements of the peptide fibrils. Increasing concentrations of copper chloride (i.e., 2.5 and 5 mM) revealed the same trend of morphological transformations before and after reduction (Figure S2 and Figure S3, respectively). EDX analysis verified the incorporation of metal ions within the cHF–nanoparticle (NP) assemblies. Alongside copper peaks, Cu^{2+}-containing samples revealed pronounced peaks for oxygen (O), indicative of a copper oxide phase (Figure 2E).

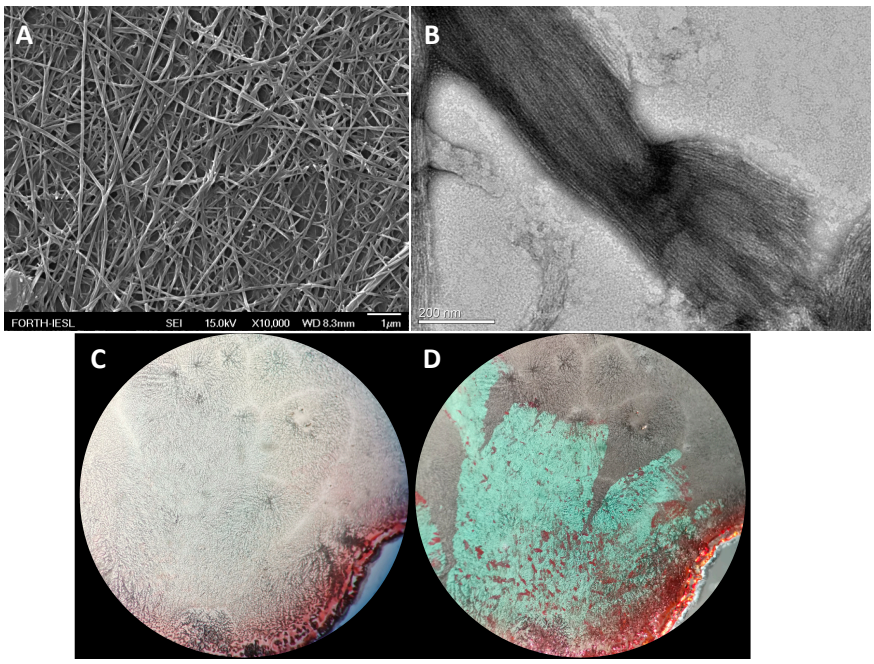

Figure 1. Images of cHF peptide in PBS at a concentration of 5 mM under (**A**) FESEM (scale bar represents 1 μm), (**B**) TEM with uranyl acetate negative staining (scale bar represents 200 nm), (**C**,**D**) Congo Red images without polarizer (**C**), under cross polarizer (**D**).

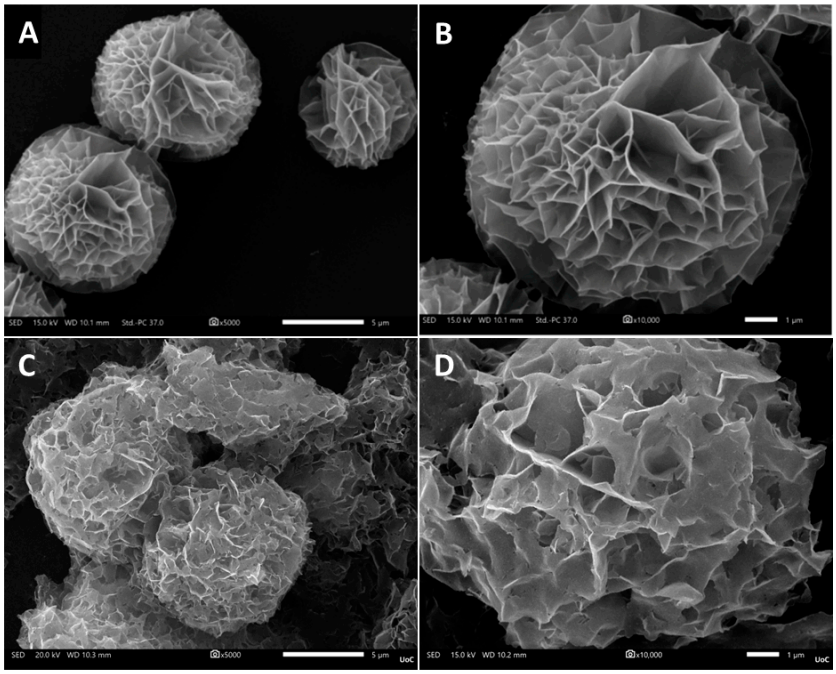

Figure 2. *Cont.*

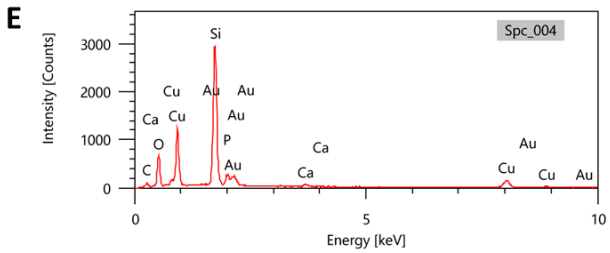

Figure 2. FESEM images of 5 mM cHF peptide complexes with 1 mM $CuCl_2$ at pH 7.4 at different magnifications ×5000 and ×10,000. (**A**,**B**) Before reduction (scale bars represent 5 µm and 1 µm, respectively), (**C**,**D**) after the addition of $NaBH_4$ (scale bars represent 5 µm and 1 µm, respectively); (**E**) representative EDX spectra of cHF–CuNPs after the reduction.

Noticeable morphological alterations of the cyclo-(His-Phe) peptide were detected upon the addition of the zinc chloride in the same range of concentrations as copper chloride, observed prior to and following reduction. A predominant characteristic of all structures obtained in the presence of zinc was the formation of amorphous to quasi-spherical assemblies in the nanoscale range. At the lowest concentration of zinc (0.5 mM), the appearance of nanostructures alongside the presence of fibrils was evident (Figure S4). At 1 mM $ZnCl_2$, spherical structures (Figure 3A,B) which became better defined upon reduction dominated (Figure 3C,D). EDX analysis of $ZnCl_2$-containing samples showed significant peaks for zinc (Zn) and oxygen (O), confirming the formation of zinc oxide structures (Figure 3E).

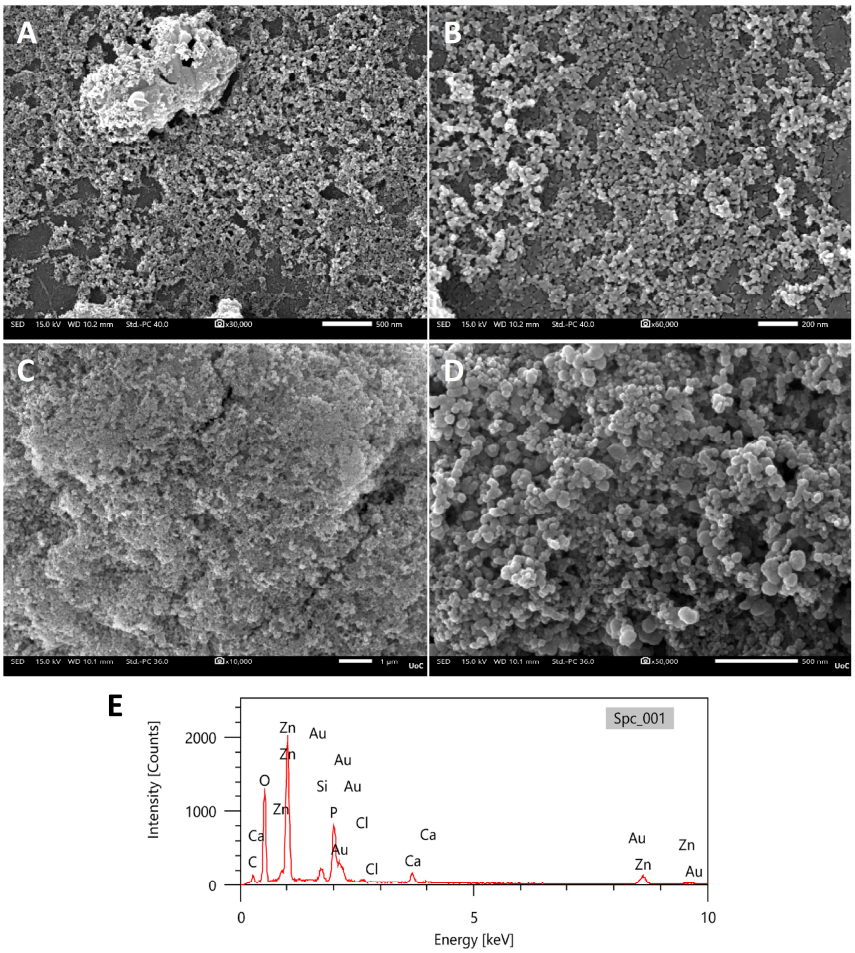

Figure 3. FESEM images of 5 mM cHF peptide upon the addition of 1 mM $ZnCl_2$ at pH 7.4 at two magnifications. (**A**,**B**) Before reduction (scale bars represent 500 nm and 200 nm, respectively),

(**C**,**D**) after the addition of $NaBH_4$ (scale bars represent 1 µm and 500 nm, respectively); (**E**) representative EDX spectra of cHF–ZnNPs after the reduction.

Increasing concentrations of zinc chloride (i.e., 2.5 and 5 mM) revealed the same trend of morphological transformations before and after reduction (Figure S5 and Figure S6, respectively).

TEM analysis of cHF–CuNPs negatively stained with uranyl acetate revealed petal-like sheets that fold upon each other and create electron-dense structures; in isolated sheets, the arrangement of electron-dense dots appears at their edges (indicated by arrows) (Figure 4A).

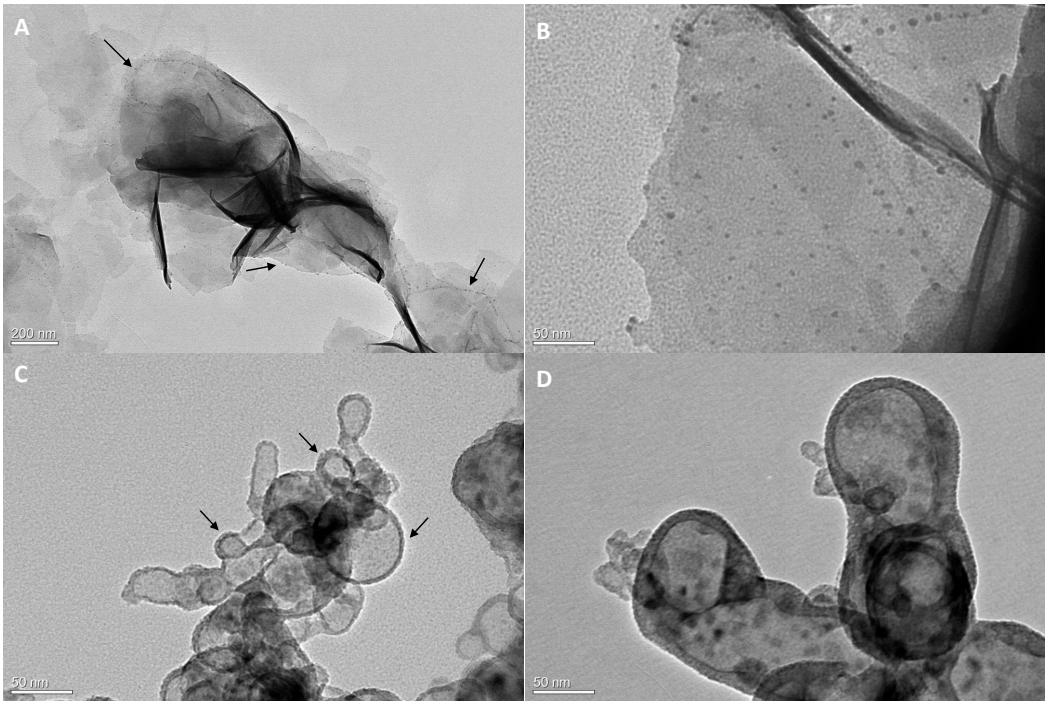

Figure 4. TEM images of cHF–CuNPs (1 mM) at different magnifications (**A**,**B**) (scale bars represent 200 nm and 50 nm, respectively), and cHF–ZnNPs (1 mM) (**C**,**D**) (scale bars represent 50 nm) at pH 7.4, negatively stained with uranyl acetate and obtained at 200 kV. Black arrows point to electron-dense dots.

cHF–ZnNPs reveal mostly bubble-like spherical morphologies, decorated with electron-dense dots at their edges (indicated by arrows) (Figure 4C). In most of the pictures, the copper–peptide "petals" or zinc–peptide "bubbles" overlap, giving very intense electron-dense areas that make it difficult to clearly distinguish details. We tried to image isolated "petals" of the flower-like structures of copper and "bubbles" for zinc. Arrays of nanoparticles seem to be arranged on the copper "petals" (Figure 4B) or enclosed within the zinc "bubbles" (Figure 4D). The arrangement of electron-dense dots probably implies an initial templating of dots that subsequently evolve/coalesce into nanoparticles.

These results confirm the role of cHF in templating copper- and zinc-based nanoparticles.

Overall, these results corroborate the coordination of Cu^{2+} and Zn^{2+} ions with cHF peptides towards forming hybrid peptide–metal nanostructures. The tendency to adopt spherical morphologies with Zn^{2+}, as compared to the more complex, flower-like structural formations with Cu^{2+}, reflects the different coordination and assembly dynamics between the peptide and these metal ions. Indeed, histidine moieties coordinate with Cu (II) ions in square planar geometry, whereas they coordinate in tetrahedral geometry with Zn

(II) ions [34]. Further, it is well established that copper and zinc nanoparticles readily oxidize in air and aqueous environments [35,36], thus explaining the oxygen peaks in the EDX patterns.

3.2. Structural Characterization with Fourier-Transform Infrared Spectroscopy (FTIR) Analysis

The self-assembled fibrils of the cHF peptide and their coordination with copper and zinc ions with the subsequent formation of NPs was assessed by solid-state Fourier-transform infrared (FTIR) spectroscopy; the spectra were recorded from 4000 to 400 cm^{-1}. In particular, the stretching mode of the C=O groups in the amide I region of the peptide backbone can be highly diagnostic for different types of secondary structures, such as α-helices, β-sheets and β turns [37]. A comparison between the FTIR spectra of peptide powder and the self-assembled cHF fibrils after lyophilization is shown in Figure 5.

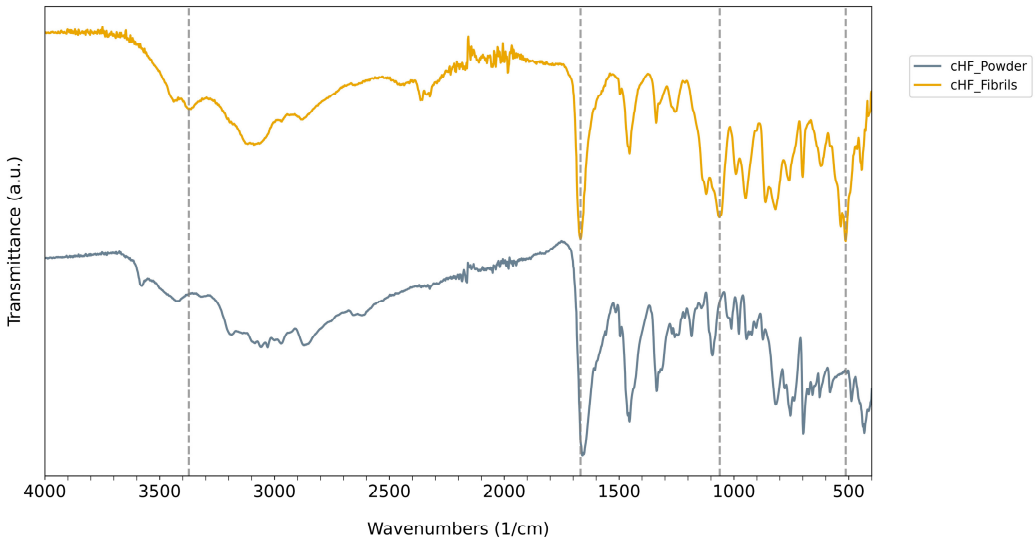

Figure 5. FTIR spectra of cHF peptide powder (gray line) and cHF fibrils after lyophilization (brown line). The vertical dashed lines indicate the main vibrational regions associated with peptide functional groups, including the broad O–H/N–H stretching region (~3400 cm^{-1}), the amide I band (~1650 cm^{-1}), the C–N stretching/N–H bending region (~1100 cm^{-1}), and the bending vibration of the N-H group (~500 cm^{-1}).

For the peptide powder (gray line), the maximum of the amide I band is at 1658 cm^{-1}, attributed to the random coil structure. In contrast, the self-assembled cHF (brown line) produces a red-shifted band at ∼1668 cm^{-1}, attributed to beta-turns [38,39], reflecting an increase in hydrogen bonding due to the peptide self-assembly in agreement with previously reported spectra [40]; of note, cyclic dipeptide assemblies lack elongated beta-sheets [41].

The FTIR spectrum of the self-assembled cHF presents a band at 3089 cm^{-1} that could be attributed to the C-H stretching vibration of the imidazole ring of histidine and a band at around 3373 cm^{-1} corresponding to N-H stretching vibration. Moreover, the bands at 1454, 1338, 1255, and 1062 cm^{-1} correspond to the imidazole group's C-N stretching and N-H bending modes. Additionally, the band at 513 cm^{-1} corresponds to the bending vibration of the N-H group [40].

The increased addition of copper (Figure 6A) and zinc ions (Figure 6B) at 0.5, 1, 2.5, and 5 mM shifts the 3373 cm^{-1} band of the cHF to 3327, 3336, 3290, and 3234, and 3350, 3317, 3353, and 3257 cm^{-1}, respectively. This shift indicates the coordination of the metals to the histidine amino acid and that higher metal concentrations cause a more considerable shift (around 100 to 130 cm^{-1}) [42]. In both cases, the peak between 3350 and 3200 cm^{-1}

became broader after the addition of metal ions. This is caused by the O-H group of H_2O on the surface of the nanostructures and, subsequently, the formation of NPs [43].

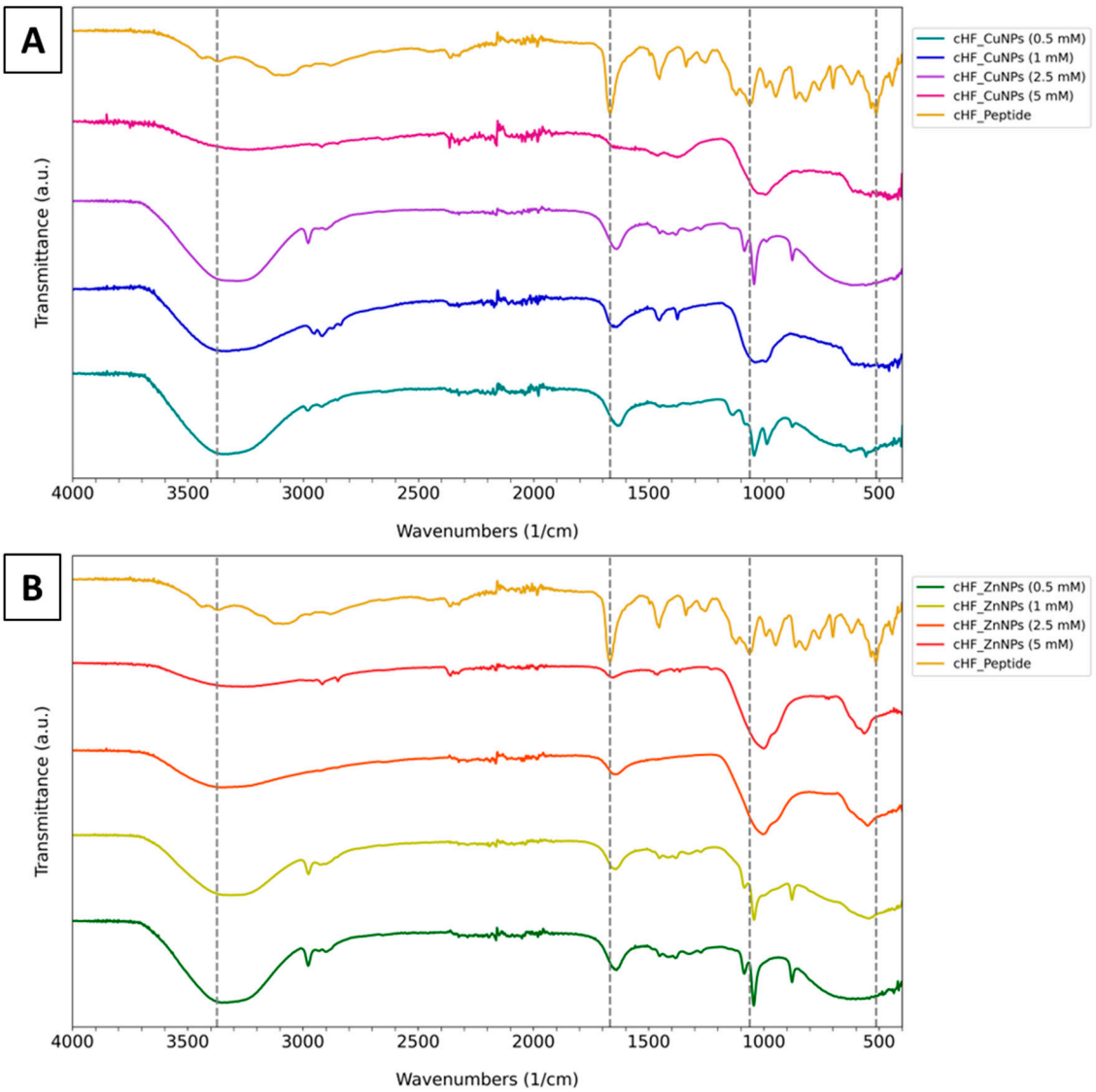

Figure 6. FTIR spectra of (**A**) cHF–CuNPs and (**B**) cHF–ZnNPs at different concentrations of 0.5, 1, 2.5 and 5 mM and the cHF peptide as control. The vertical dashed lines indicate the main vibrational regions associated with peptide functional groups, including the broad O–H/N–H stretching region (~3400 cm^{-1}), the amide I band (~1650 cm^{-1}), the C–N stretching/N–H bending region (~1100 cm^{-1}), and the bending vibration of the N-H group (~500 cm^{-1}).

Moreover, the band at 1668 cm^{-1} was shifted to 1640, 1642, 1642, and 1654 cm^{-1}, and 1629, 1639, 1639, and 1660 cm^{-1}, respectively, with increasing copper and zinc ion concentrations. As mentioned above, the addition of low ion concentration (0.5 mM) shifts the amide I band toward a lower frequency, reflecting an increase in hydrogen bonding due to the rise in an ordered secondary structure [44]. However, further increasing of the metal ion concentrations did not shift the wavelength significantly, meaning that they do not give rise to more packed beta-sheets but contribute to the observed spherical formations. We cross-validated the configuration modifications via our observations using FESEM. As an example, the addition of a small quantity of copper chloride up to 0.5 mM led to the formation of a more refined and compact fibril network (as depicted in Figure S1A,B). Conversely, concentrations of copper chloride higher than 0.5 mM produced spherical for-

mations (as evidenced in Figure 2). Furthermore, the shift or the absence of the bands 1454, 1338, and 1255 cm^{-1} might indicate the role of the cHF peptide as a stabilizing/templating agent and the structural transformation of the formed assemblies during the formation of metal particles. Lastly, the formation of metal complexes caused the shift in band at 1062 cm^{-1} by 20 to 60 cm^{-1} [42]. The shift in the sharp peak at 513 cm^{-1} indicates the coordination of histidine with Cu and Zn since it corresponds to N-H vibration. Additionally, the band becomes broader and weaker in high concentrations of metals. Moreover, the increased amount of zinc ions led to a new broad peak at 563 cm^{-1}, which can be attributed to the stretching/vibration of the metal–oxygen bond in Zn–O due the formation of ZnO NPs [45–47].

3.3. Antibacterial Properties of the cHF and cHF–Metal Complexes

The FTIR method confirmed the ability of the cHF peptide to coordinate successfully with the histidine residues, leading to the efficient formation of cHF–CuNP and cHF–ZnNP complexes. These samples were tested against the Gram-negative bacteria *E. coli* and Gram-positive bacteria *S. aureus*. In both cases, the pristine cHF peptide did not show any antimicrobial activity. However, the antimicrobial effectiveness of these metal ions can be affected when they form complexes with the peptides [48]. The antimicrobial efficiency of cHF–metalNPs showed a concentration dependence for both copper and zinc, as shown in Figure 7.

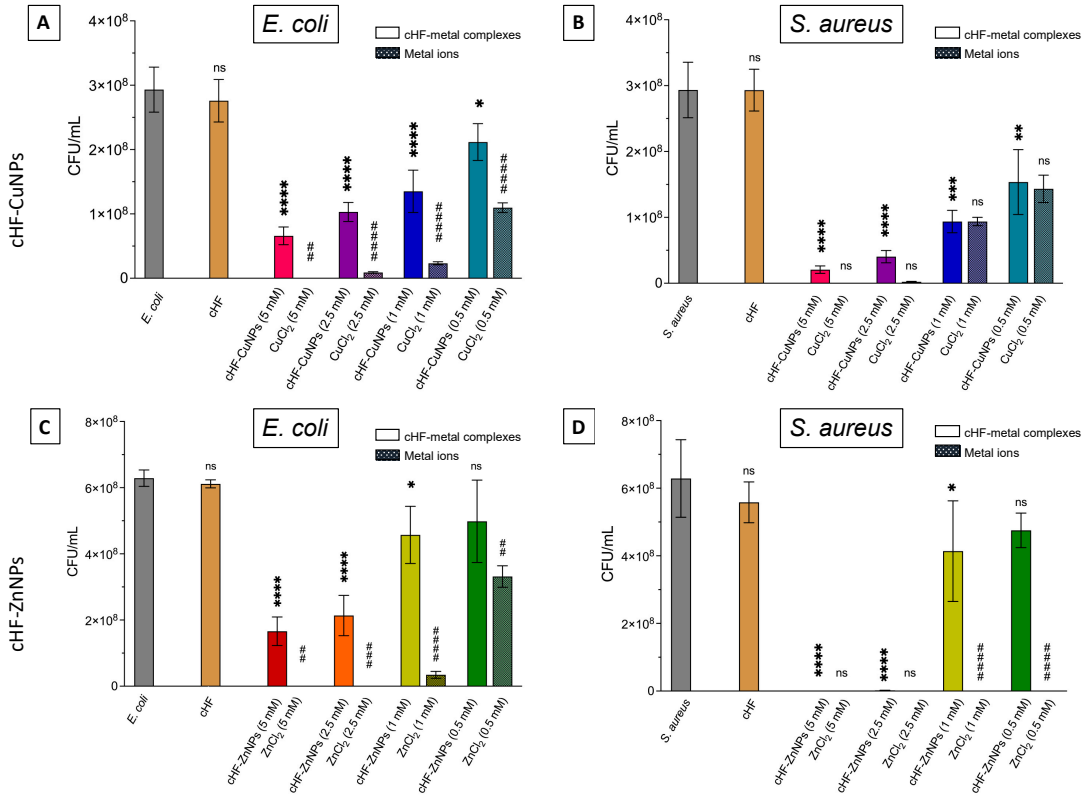

Figure 7. CFU/mL quantification of *E. coli* (**A**,**C**) and *S. aureus* (**B**,**D**) following treatment with cHF and cHF–CuNPs and cHF–ZnNPs complexes at the concentrations of 5, 2.5, 1 and 0.5 mM (solid bars), and the corresponding concentrations of their metal ions ($CuCl_2$ and $ZnCl_2$) used as controls (patterned bars). (**A**,**B**) show treatment with copper peptide complexes and corresponding ions, whereas (**C**,**D**) show treatment with the zinc counterparts. Non-visible bars indicate values close to 0. Statistical significance relative to the untreated cells is indicated as * $p < 0.05$, ** $p < 0.01$, *** $p < 0.001$, **** $p < 0.0001$; ns denotes non-significance. Differences between cHF–metal complexes and their corresponding metal ions are shown as ## $p < 0.01$, ### $p < 0.001$, #### $p < 0.0001$.

Specifically, the bacteriostatic activity of cHF–CuNPs against *E. coli* ranged from 20% to 70%, depending on the concentration, while $CuCl_2$ exhibited stronger inhibition, ranging from 70% to nearly 100%. In parallel, cHF–CuNPs showed bacteriostatic effects between 5% and 50% against *S. aureus*, comparable to those of $CuCl_2$. Similar to cHF–CuNPs, cHF–ZnNPs showed higher bacteriostatic activity against *S. aureus* than *E. coli.* In particular, cHF–ZnNPs inhibited *E. coli* growth by 20% to 80% in a concentration-dependent manner, whereas $ZnCl_2$ exhibited stronger inhibition, ranging from 50% to nearly 100%. Against *S. aureus*, cHF–ZnNPs at higher concentrations (5 mM and 2.5 mM) resulted in near complete inhibition, while at lower concentrations (1 mM and 0.5 mM), bacterial survival remained at approximately 70 to 80%. In contrast, free zinc ions induced complete growth inhibition of *S. aureus* against all tested concentrations.

3.4. In Vitro Cytotoxicity of cHF–Metal Complexes on Fibroblasts

Low cytotoxicity of nanoparticles (NPs) on human cells is a crucial requirement for their use in therapeutic applications. Hence, we evaluated the cytotoxicity of the cHF–CuNPs and cHF–ZnNPs on the L292 fibroblasts (Figure 8) at 24 h and 48 h, with the corresponding concentrations of copper and zinc chloride used as controls. This assessment determines their potential applicability as therapeutic agents with antimicrobial activity.

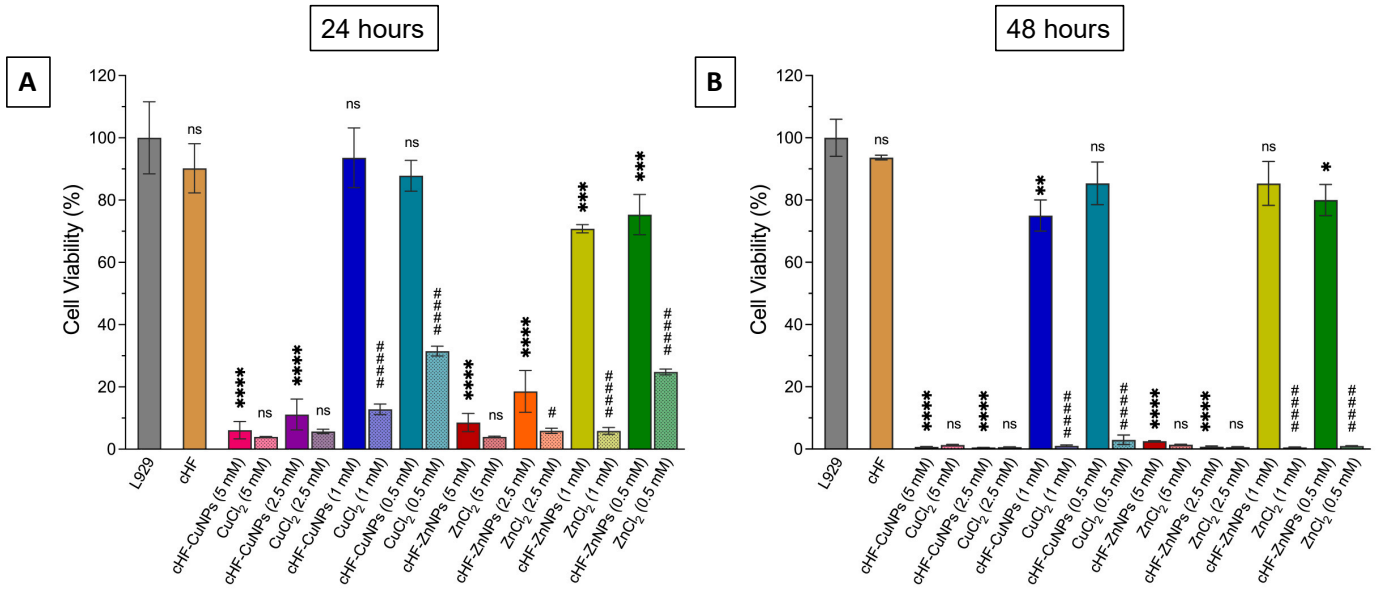

Figure 8. Cell viability assessment using L929 fibroblast following treatment with cHF, cHF–CuNPs, cHF–ZnNPs, and the corresponding concentrations of metal ions used as controls at (**A**) 24 h and (**B**) 48 h. Data are presented as mean ± SD ($n \geq 4$). Statistical significance relative to the untreated cells is indicated as * $p < 0.05$, ** $p < 0.01$, *** $p < 0.001$, **** $p < 0.0001$; ns denotes non-significance. Differences between cHF–metal complexes and metal ions are shown as # $p < 0.05$, #### $p < 0.0001$.

The peptide cHF did not significantly affect the viability of the fibroblast L929 cell line at either time point. However, in the presence of 5 mM and 2.5 mM of $CuCl_2$ and $ZnCl_2$ in the formed cHF–CuNPs and cHF–ZnNPs, pronounced cytotoxicity was observed, with cell viability decreasing to approximately 5–10% at 24 h and becoming almost undetectable at 48 h. On the contrary, treatment with cHF–CuNPs at 1 mM reduced cell survival from 94 ± 9% at 24 h to 75 ± 5% at 48 h. Treatment with cHF–CuNPs at 0.5 mM decreased the cell viability to around 80% at both time points, indicating no further reduction beyond 24 h. Interestingly, at the same concentrations (0.5 and 1 mM $ZnCl_2$), cHF–ZnNPs caused a more pronounced decrease in cell viability to 70 ± 1% and 75 ± 6% at 24 h, respectively (Figure 8A). However, at 48 h (Figure 8B), the survival of L929 cells increased to 80–85%, in-

dicating a time-dependent recovery at lower metal concentrations. Furthermore, treatment with $CuCl_2$ and $ZnCl_2$ alone resulted in an almost complete loss of viability of L929 cells across all tested concentrations and both time points, except for 0.5 mM $CuCl_2$ and $ZnCl_2$ at 24 h, where cell survival remained at 30%.

3.5. In Vitro Cytotoxicity of cHF–Metal Complexes on Human Osteosarcoma Cells

The in vitro effect of the cHF–CuNPs and cHF–ZnNPs on the cell viability was studied in MG-63 osteosarcoma cancer cells at pH 7.4 for 24 h (Figure 9A) and for 48 h (Figure 9B). The treated MG-63 cells with cHF peptide alone did not affect cell viability after 24 h and 48 h. In contrast, cHF–CuNPs and cHF–ZnNPs at 5 mM caused the near-complete loss of cell viability (1–3%). However, decreasing concentrations of $CuCl_2$ or $ZnCl_2$ to 2.5 mM led to a statistically significant difference in survival depending on the metal ion. Specifically, the cHF–CuNPs reduced viability to 58 $\pm$ 2%, whereas the presence of the cHF–ZnNP complex showed a more potent effect against MG-63, reducing cell survival to 31 $\pm$ 2%. However, the differences were minor when the complexes with 0.5 and 1 mM of $CuCl_2$ and $ZnCl_2$ were tested. In particular, the survival of the MG-63 cells remained between 50 and 70% within the first 24 h, while an increase in cell survival was observed at 48 h, confirming the time-dependent recovery at lower metal concentrations. Moreover, treatment with $CuCl_2$ and $ZnCl_2$ caused an almost complete loss of the viability of MG-63 cells at pH 7.4 and across all tested concentrations and both time points, except for 0.5 mM $CuCl_2$, in which cell viability values of 80 to 60% were observed, depending on time.

Nevertheless, the in vitro physiological conditions at pH 7.4 do not fully replicate the osteosarcoma microenvironment, including acidosis and hypoxia [49]. Therefore, to emulate the osteosarcoma environment in vitro, we performed the same experiments at pH 6.4 at 24 h (Figure 9C) and at 48 h (Figure 9D). The cHF peptide did not show any change in the survival of MG-63 cells at pH 6.4 after 24 h. As observed under physiological conditions, only minimal cell survival was detected in the presence of 5 mM cHF–CuNPs and cHF–ZnNPs. Notably, acidic conditions enhance the release of metal ions, leading to a more pronounced difference in MG-63 cell survival between the two metal ions and highlighting the metal-dependent cytotoxic effect. At 0.5, 1, and 2.5 mM of $CuCl_2$, the cHF–CuNP complexes reduced the cell viability of MG-63 to 25 $\pm$ 5%, 50 $\pm$ 18%, and 65 $\pm$ 10% at 24 h, respectively, while cell viability was further decreased at 48 h. In contrast, under similar treatment conditions, the cHF–ZnNP complexes resulted in higher cytotoxicity, with a survival of MG-63 between 5 and 10% at 24 h and 48 h. The only exception was treatment with 0.5 mM of cHF–ZnNPs, for which the cell survival increased significantly at 48 h. The addition of $CuCl_2$ or $ZnCl_2$ as controls led to extremely high cell toxicity rates under all different concentrations and time points.

3.6. Morphological Analysis of cHF–CuNPs and cHF–ZnNPs and Ion-Induced Osteosarcoma Cells

Furthermore, we investigated whether the morphology of nanoparticles initially prepared at pH 7.4 (as described in Section 2.3.5) changes after being resuspended in mildly acidic conditions (pH 6.4) for 24 h. For the cHF–CuNPs, flower-like structures were not observed; instead, much smaller amorphous formations appeared (Figure 10A,B). EDX spectra confirmed the presence of copper oxide (Figure 10C). For the cHF–ZnNPs, the structures appeared rather amorphous compared to the well-formed spherical formations at pH 7.4; bundles of fibrils could also be observed (Figure 10D,E). EDX spectra confirmed the presence of zinc oxide (Figure 10F) phases. Overall, the above results suggest that cHF nanoparticle complexes dissociate upon transfer to pH 6.4, resulting in smaller formations and even peptide fibril structures. As a result, metal nanoparticles are released upon contact with the acidic tumor microenvironment, resulting in higher cytotoxic activity at this pH.

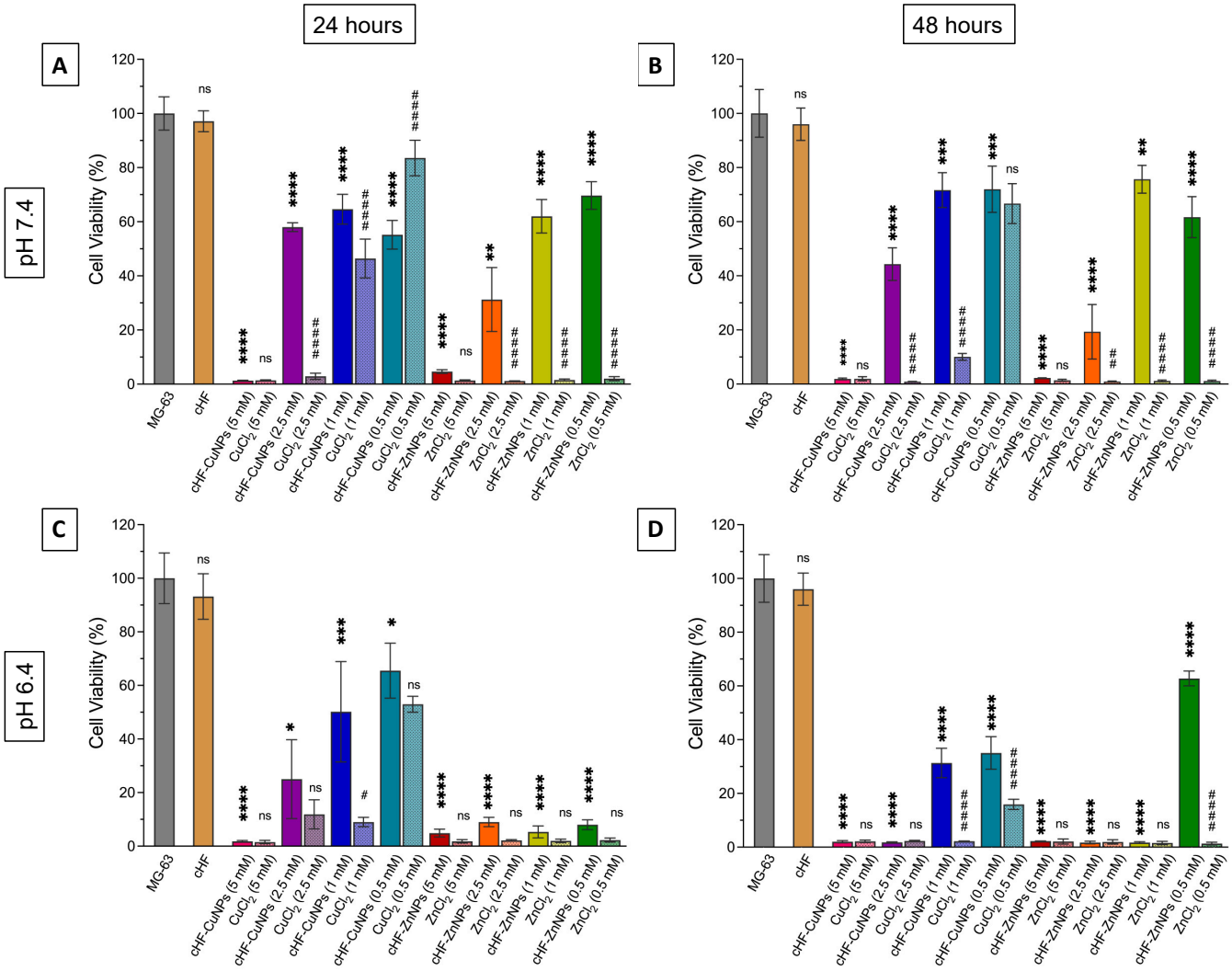

Figure 9. Cell viability assessment using MG-63 osteosarcoma cells following treatment with cHF, cHF–CuNPs, cHF–ZnNPs, and the corresponding concentrations of metal ions used as controls. Experiments were performed under physiological conditions at pH 7.4 at (**A**) 24 h and (**B**) 48 h, and at pH 6.4 at (**C**) 24 h and (**D**) 48 h. Data are presented as mean ± SD ($n \geq 4$). Statistical significance relative to the untreated cells is indicated as * $p < 0.05$, ** $p < 0.01$, *** $p < 0.001$, **** $p < 0.0001$; ns denotes non-significance; differences between cHF–metal complexes and metal ions are shown as # $p < 0.05$, ## $p < 0.01$, #### $p < 0.0001$.

In a more direct approach, MG-63 osteosarcoma cells were treated with cHF (5 mM) and cHF–CuNPs and cHF–ZnNPs (1 mM) to evaluate the changes in the cell morphology (Figure 11). The FESEM images of untreated cells indicate their physiological morphology (Figure 11A), similar to the cells treated with the cHF peptide (Figure 11B), which exhibited normal morphology. In contrast, cells treated with cHF–CuNPs (Figure 11C) and cHF–ZnNPs (Figure 11D) appeared highly deformed, suggesting cell damage or death.

Alongside the FESEM observations, the EDX analysis confirmed the presence of metal ions on the cells, as shown in Figure 11E,F, suggesting that metal ions may be responsible for the cell damage, most probably due to the disruption of the cell membranes.

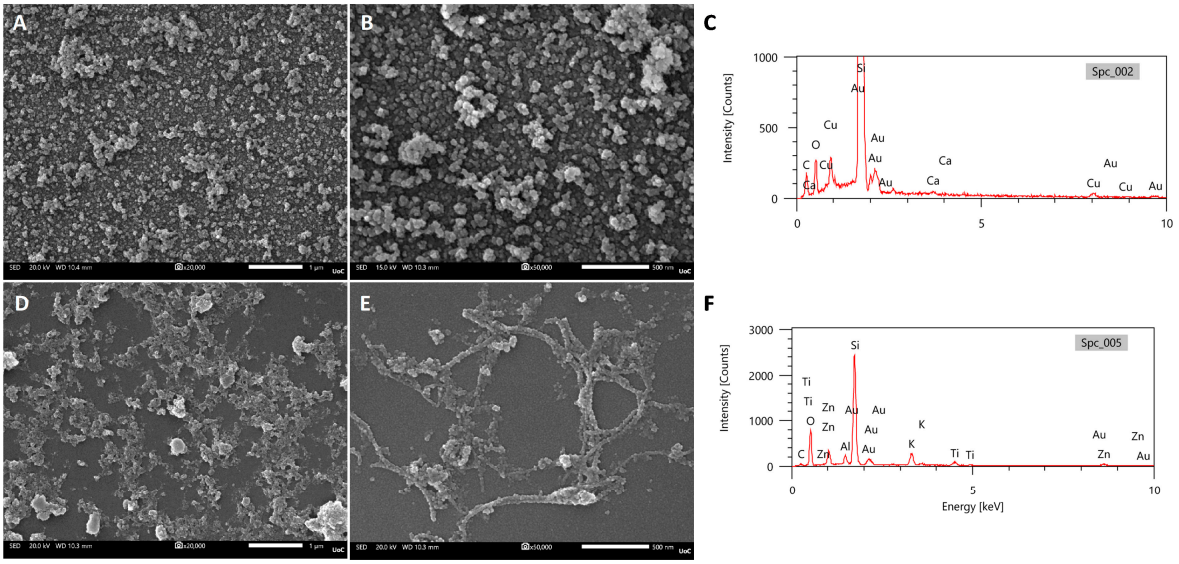

Figure 10. (**A**,**B**) FESEM images of cHF–CuNPs (1 mM) at pH 6.4 at different magnifications, (**C**) representative EDX spectra of cHF–CuNPs. (**D**,**E**) FESEM images of cHF–ZnNPs (1 mM) at pH 6.4 at different magnifications, and (**F**) representative EDX spectra of cHF–ZnNPs. Scale bars represent 1 µm in (**A**,**D**) and 500 nm in (**B**,**E**).

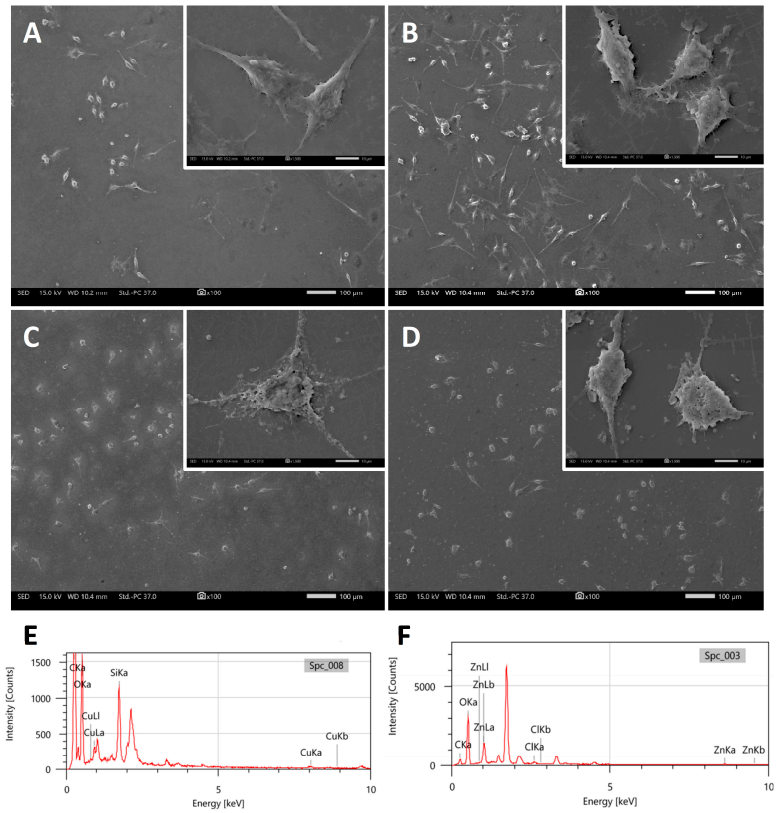

Figure 11. Representative FESEM images showing MG-63 cells at pH 6.4. (**A**) Untreated cells, (**B**) cells in the presence of the cHF peptide (5 mM), (**C**) cells in the presence of the cHF–CuNPs (1 mM), (**D**) cells in the presence of the cHF–ZnNPs (1 mM). Representative EDX analysis on MG-63 cells treated with (**E**) cHF–CuNPs, (**F**) cHF–ZnNPs. Scale bars in (**A**–**D**) represent 100 µm. Inserts display higher magnification images with scale bars at 10 µm.

3.7. Measurement of Generated ROS

Furthermore, the generation of intracellular ROS induced by cHF–metal nanoparticles was evaluated using the DCFDA assay, which is a cell-permeable and non-fluorescent probe that is rapidly deacetylated by intracellular ROS to the highly fluorescent 2′,7′-dichlorofluorescein (DCF), enabling the quantitative evaluation of oxidative stress (Figure 12).

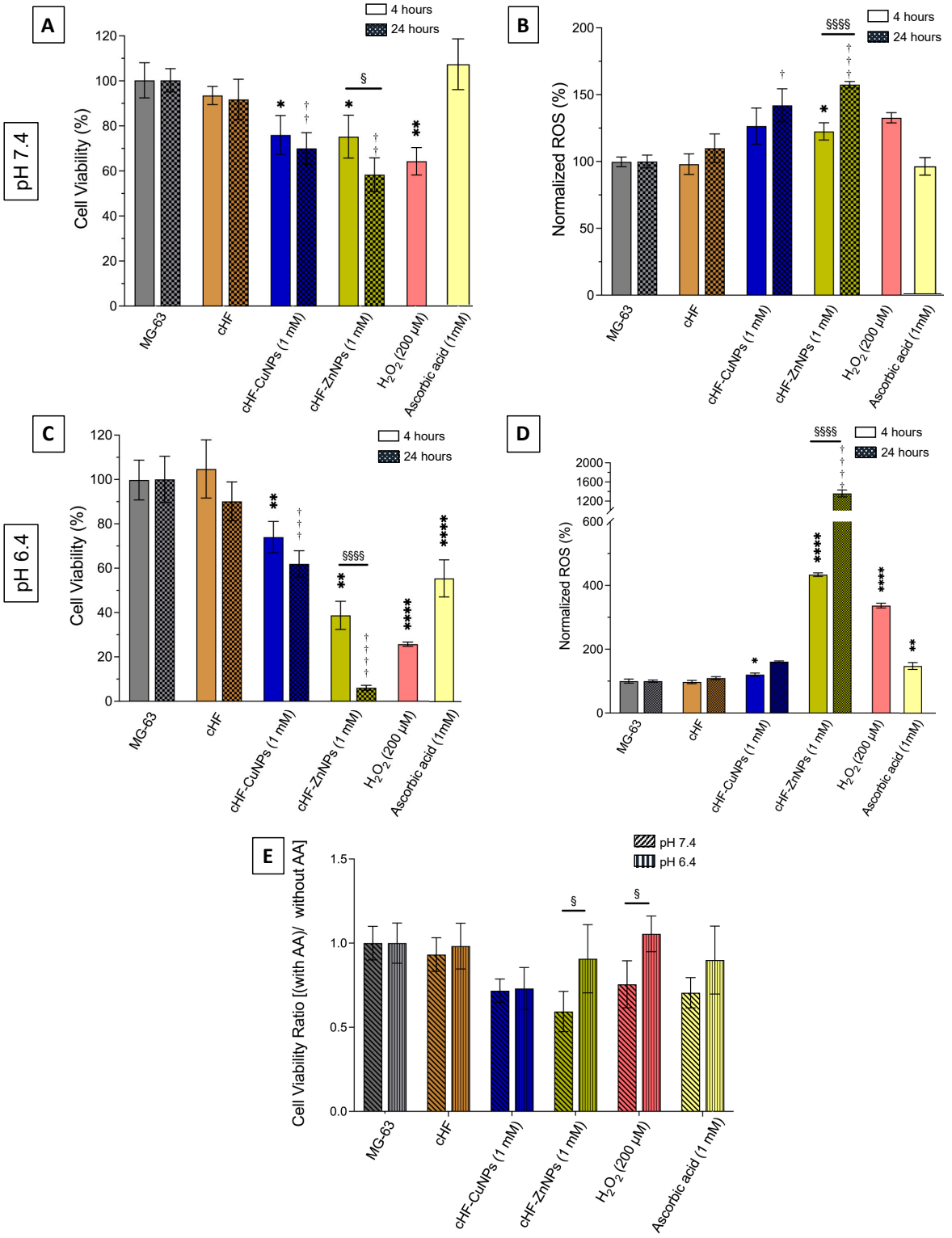

Figure 12. (**A**,**C**) Cell viability, (**B**,**D**) ROS normalized by cell viability at (**A**,**B**) pH 7.4 and (**C**,**D**) pH 6.4 in MG-63 osteosarcoma cells following treatment for 4 h (solid) and 24 h (patterned) with cHF

peptide, cHF–CuNPs (1 mM), cHF–ZnNPs (1 mM), ascorbic acid, and H_2O_2. Statistical significance of differences is presented between the cHF complexes and the untreated cells at 4 h (designated with *), between cHF complexes and untreated cells at 24 h (designated with †), and between 4 and 24 h at the same peptide complex concentration (designated with §). The symbols *, †, and § indicate $p < 0.05$; **, †† $p < 0.01$; ††† $p < 0.001$; ****, ††††, §§§§ $p < 0.0001$. (**E**) Rescue experiment following treatment with AA for 1 h is expressed as cell viability ratio (after AA treatment)/without AA) at pH 7.4 and pH 6.4. Data are presented as mean ± SD ($n \geq 4$). Ascorbic acid and hydrogen peroxide were used as negative and positive controls, respectively. Statistical analysis of differences between pH 7.4 and 6.4 are designated with § ($p < 0.05$).

To demonstrate the action of cHF–metal complexes on cancer cells, we studied the cell viability (Figure 12A) and intracellular ROS production (Figure 12B) in MG-63 osteosarcoma cells at pH 7.4 and at pH 6.4 (Figure 12C,D) after 4 and 24 h. MG-63 cells treated with cHF peptide retained viability close to control levels at both 4 and 24 h, indicating that the peptide itself does not exert cytotoxic effects. In contrast, treatment with cHF–CuNPs and cHF–ZnNPs resulted in a clear reduction in cell viability, which became more pronounced at 24 h. It was observed that cHF–CuNPs caused a moderate decrease in cell viability, whereas cHF–ZnNPs caused a stronger and delayed loss of viability. In parallel, intracellular ROS levels of MG-63 cells treated with the cHF peptide remained near physiological levels, while both cHF–CuNPs and cHF–ZnNPs significantly increased ROS generation, in particular at 24 h. Among them, cHF–ZnNPs induced the highest ROS levels, according to their stronger cytotoxic effect. These results suggest that the cytotoxic effects observed after treatment with cHF–metal complexes are primarily mediated by oxidative stress and are both time- and metal-dependent.

Moreover, to directly assess whether oxidative stress was responsible for the observed decrease in cell viability, a rescue experiment was performed using ascorbic acid (Figure 12E). We calculated the cell viability ratio in the presence versus in the absence of ascorbic acid. The results demonstrate that there is no effect in the untreated cells, as no oxidative damage was present, as well as in cells treated with the cHF peptide. Although no recovery of cell viability was observed, as the calculated ratios are below the value of 1, the significantly increasing viability ratios in cHF–ZnNPs-treated cells and in H_2O_2 at pH 6.4 compared to pH 7.4 indicate an effect of ascorbic acid to zinc-associated cytotoxicity. It is noteworthy that cHF–ZnNPs induced a high ROS production, associated with high cytotoxicity, confirming that oxidative damage often leads to irreversible changes and cell death even after antioxidant intervention.

4. Discussion

Over the past decade, nanocarrier-based drug delivery systems, especially peptides and proteins, have been the subject of exhaustive research, presenting novel avenues for therapeutic interventions [50]. Specifically, in the context of osteosarcoma, recent advances in targeted drug delivery systems have been reported [51]. Metal nanoparticle carriers have the potential to advance treatment methods by enhancing selective targeting, improving treatment efficacy, and potentially reducing side effects [52]. Application of chitosan-capped CuNPs against MG-63 osteosarcoma cells has been reported [53]. Very recently, histidine-containing octa and decapeptides from angiogenin were proven to chelate copper (II) ions and evaluated against normal osteoblast cells and osteosarcoma cells. Interestingly, the peptides alone were not cytotoxic against both cell lines, whereas their complexes with copper were cytotoxic only against osteosarcoma cells [54]. The field of minimal peptide carriers (e.g., dipeptides) for osteosarcoma drug delivery still merits being explored.

The pursuit of understanding the interaction of peptides with metal ions, particularly within the context of cyclic peptides, has evolved into an exciting field [55] with promising biological applications [26]. In the present study, we have chosen to study the relatively

unexplored cHF peptide, in terms of its self-assembling propensity and as a chelating agent to assemble stabilized copper and zinc peptide composite nanoparticles. The cHF peptide self-assembles into fibrils upon its dissolution in PBS, with FESEM and Congo Red staining confirming the characteristic amyloid fibril signature. Initially, we tested whether cHF self-assembled fibrils could affect the cell viability of the MG-63 cancer cells, as anticancer properties have been reported for cyclic dipeptides [56]. Previous studies demonstrated significant inhibition by cHF in the growth of the cancer cell lines of HeLa, MCF-7, and WHCO3 at 1 mM [30]; however, the cHF peptide has not been previously tested on of MG-63 cancer cells and did not affect their viability as shown in the present study.

Our subsequent experiments affirmed the peptide ability to chelate metal ions, specifically copper and zinc, leading to the synthesis of cHF–CuNPs and cHF–ZnNPs upon reduction. FESEM imaging showed that the complexing of the cHF peptide exerts a modulatory effect on morphology, particle size and distribution [47]. Intriguingly, the cHF–CuNPs have led to the formation of flower-like structures consisting of thin nanosheets. Such morphologies of copper oxide nanostructures have previously been synthesized employing "green" chemistry [57]. Alternatively, the cHF–ZnNPs showed spherical morphologies with heterogeneous size distribution, where increased concentrations of zinc ions led to enlarged sphere sizes. TEM confirmed the presence of distinct metal nanoparticles templated on peptide sheets and fibrils; FTIR spectroscopy confirmed the structural changes induced by the interaction of peptide fibrils with copper and zinc.

Antimicrobial peptides were reported to also have anticancer activity [58,59]. Given that the cHF peptide was previously reported to have anticancer activity on a few cancer cell lines [30], we tested the antimicrobial activities of the peptide alone and metal ion–cHF complexes compared to metal ions alone. We explored the eventual antimicrobial activity against *E. coli* Gram-negative bacteria and *S. aureus* Gram-positive bacteria. The cHF peptide itself did not show a notable antibacterial effect against *E. coli* and *S. aureus*, in contrast to the previously reported cHF higher effectiveness against Gram-negative bacteria and lower activity against Gram-positive; however a direct comparison is not feasible, since these antimicrobial assays were carried out with the disk diffusion method [30].

Metal nanoparticles can adopt various morphologies including nanorods, nanotubes, nanobelts, nanoplates, nanorings, and even intricate designs such as "nanoflowers". As previously suggested, these morphological variations can substantially influence the antimicrobial activity of nanoparticles. Indeed, several studies have indicated that the particle shape and size can influence the antibacterial activity of copper NPs. Amongst these, the flower-like ones proved to be the most potent due to their larger surface area and different structure, which can affect various cellular components of microbial cells [60]. Indeed, the flower-like structured cHF–CuNPs displayed a concentration-dependent bacteriostatic activity. Specifically, against *E. coli*, the bacteriostatic activity ranged from 20% to 70%, while against *S. aureus*, it varied between 5% and 50; the results demonstrate that as the concentration of these nanoparticles increased, their antibacterial efficacy also increased. The antimicrobial effectiveness of CuO nanoparticles in the 100 to 5000 mg/mL concentration has previously been reported against *S. aureus* and *E. coli* [61]. cHF–ZnNPs exhibited higher bacteriostatic efficiency against *S. aureus* than against *E. coli.* At 5 mM and 2.5 mM, cHF–ZnNPs caused almost complete death of *S. aureus* cells, while at 1 mM it remained at 70–80%. Therefore, both cHF–NPs demonstrated antimicrobial efficiency at the concentration of 1 mM.

For potential therapeutic applications, both cHF–CuNPs and cHF–ZnNPs must demonstrate biocompatibility in vitro. At high concentrations (5 and 2.5 mM), cHF–CuNPs and cHF–ZnNPs caused significant cytotoxicity in the L929 fibroblast cell line. Therefore, while both NPs at higher concentrations of metal ions (5 mM and 2.5 mM) showcase high efficacy

against bacterial strains, their pronounced cytotoxicity precludes them from therapeutic applications. On the other hand, cHF–CuNPs and cHF–ZnNPs of 0.5 mM may be cytocompatible but lack significant antimicrobial potency. Remarkably, both cHF–CuNPs and cHF–ZnNPs at a concentration of 1 mM strike a balance, exhibiting both biocompatibility and antimicrobial efficiency, albeit a reduced antimicrobial efficiency than their "naked" metal ion counterparts. Any antimicrobial activity would be an additional advantage, in order to protect the surrounding area from post-surgery and chemotherapy infections. This positions them as the most promising candidates for further investigations.

Finally, both cHF–CuNPs and cHF–ZnNPs showed a cytotoxic effect on MG-63 cells at pH 7.4; the effect was particularly pronounced when the pH of the cell culture decreased to 6.4, mimicking the TME. At the concentration of 1 mM, the cHF–CuNPs significantly decreased cell survival by an additional 15%, while cHF–ZnNPs reduced the survival rate by an additional 50%. This significant difference between copper and zinc nanoparticles may be partially attributed to the higher solubility of ZnO NPs in cell culture media [62]. To summarize, the cHF–metalNPs convey compelling cytotoxicity against MG-63 osteosarcoma cells at mildly acidic conditions (pH 6.4). This cytotoxicity can be attributed to an increased release of metal ions on the target cells due to the protonation of the peptide histidine imidazole group.

Particularly, redox active metal ions such as copper ions can convert hydrogen peroxide into highly reactive hydroxyl radicals, while non-redox active metal ions such as zinc ions, although they do not generate ROS directly, impair mitochondrial electron transport and deplete endogenous antioxidants, leading to the disruption of cell redox homeostasis [63]. The increased levels of ROS in osteosarcoma cells observed in this study, which are associated with the cytotoxic effects of both cHF–metal complexes at the concentration of 1 mM, confirm that intracellular ROS accumulation correlates with the activation of apoptosis. Ascorbic acid (AA) has been used as a ROS scavenger that reduces oxidative stress and can partially restore cell viability in various in vitro models when used at physiological and pharmacological concentrations, with the pharmacological concentrations killing cancer but not normal cells [64]. Previous studies [65] have shown that treatment with AA can suppress the accumulation of intracellular ROS and reverse the oxidative damage caused by metal ions or nanoparticles, particularly in zinc-containing NPs [33]. The lack of rescue by AA for cHF–CuNPs may be attributed to its role as a pro-oxidant by reducing Cu(II) to Cu(I), thereby maintaining the redox cycle of Cu ions and ROS generation, and limiting the recovery of cell viability [66]. In contrast, cHF–ZnNPs' cytotoxicity is primarily mediated through indirect mechanisms such as mitochondrial dysfunction, the disruption of antioxidant defenses, and ion-induced cellular stress, which are not readily reversible by direct ROS scavenging. As the effect of AA has been reported to be concentration-dependent [65], acting as a ROS scavenger at low concentrations and as a ROS generator at higher pharmacological doses, future studies may focus on the exploration of the rescue effect of AA in metalNPs complexes in a concentration-dependent manner towards the modulation of oxidative stress, redox-sensitive signaling pathways, and the chelation of metal ions.

5. Conclusions

In summary, the study of the histidine-containing cyclic peptide cHF and its interaction with metal ions reveals promising potential for antimicrobial applications and therapeutic strategies against osteosarcoma cells. This study demonstrates the self-assembling ability of cHF and its efficient chelation of copper and zinc ions, leading to the formation of stable metal nanoparticles with distinct morphologies. Although their efficiency against bacterial strains was observed, the cytotoxicity on mammalian cells at metal concentrations higher than 1 mM must be considered for future therapies. Nevertheless, at metal concentrations

of 1 mM, cHF–CuNPs and cHF–ZnNPs emerge as promising candidates, demonstrating a subtle balance between biocompatibility and antimicrobial potency, and underscoring the need for exploring the optimal conditions for anti-osteosarcoma applications. Furthermore, this work highlights the potential of cyclic peptides containing histidine as versatile carriers for the targeted delivery of metal ions against osteosarcoma treatment. Finally, the combination of cHF–metal nanoparticles with conventional anticancer drugs may offer a promising strategy for synergistic osteosarcoma therapies in the future.

Supplementary Materials: The following supporting information can be downloaded at: https://www.mdpi.com/article/10.3390/biom16020284/s1, Figure S1: FESEM images of the peptide cHF with 0.5 mM $CuCl_2$, Figure S2: FESEM images of the peptide cHF with 2.5 mM $CuCl_2$, Figure S3: FESEM images of the peptide cHF with 5 mM $CuCl_2$, Figure S4: FESEM images of the peptide cHF with 0.5 mM $ZnCl_2$, Figure S5: FESEM images of the peptide cHF with 2.5 mM $ZnCl_2$, Figure S6: FESEM images of the peptide cHF with 5 mM $ZnCl_2$.

Author Contributions: Conceptualization, C.P.A. and A.M.; methodology, C.P.A., G.C., A.G., M.C. and A.M.; validation, C.P.A., G.C., A.G., M.C. and A.M.; investigation, C.P.A., A.G. and G.C.; resources, M.C. and A.M.; data curation, C.P.A., A.G., M.C. and G.C.; writing—original draft preparation, C.P.A. and A.M.; writing—review and editing, C.P.A., G.C., M.C. and A.M.; supervision, M.C. and A.M.; project administration, A.M.; funding acquisition, A.M. All authors have read and agreed to the published version of the manuscript.

Funding: C.P.A. acknowledges support from the Hellenic Foundation for Research and Innovation (HFRI) under the HFRI PhD Fellowship grant (Fellowship Number: 390). C.P.A. was also co-financed by Greece and the European Union (European Social Fund-ESF) through the Operational Program "Human Resources Development, Education and Lifelong Learning" in the context of the Act "Enhancing Human Resources Research Potential by undertaking a Doctoral Research" Sub-action 2: IKY Scholarship Program for PhD candidates in the Greek Universities. A.M. and C.P.A. acknowledge support from the Stavros Niarchos Foundation (SNF) and the Hellenic Foundation for Research and Innovation (H.F.R.I.) under the 5th Call of "Science and Society" Action—"Always Strive for Excellence—Theodore Papazoglou" (Project Number: 9578, NAIAD).

Institutional Review Board Statement: Not applicable.

Informed Consent Statement: Not applicable.

Data Availability Statement: The original contributions presented in this study are included in the article/Supplementary Material. Further inquiries can be directed to the corresponding author.

Acknowledgments: The authors would like to thank Aleka Manousaki and Stefanos Papadakis for their expert technical assistance with the FESEM and SEM, respectively. We would also like to thank Sevasti Papadogiorgaki for expert technical assistance with the TEM.

Conflicts of Interest: The authors declare no conflicts of interest.

Abbreviations

The following abbreviations are used in this manuscript:

AA	Ascorbic acid
TME	Tumor microenvironment
ROS	Reactive oxygen species
cHF	Cyclic-(His-Phe)
cHF–CuNPs	Cyclic-(His-Phe)–copper nanoparticles
cHF–ZnNPs	Cyclic-(His-Phe)–zinc nanoparticles
FESEM	Field-emission scanning electron microscopy

TEM	Transmission electron microscopy
FTIR	Fourier-transform infrared spectroscopy
DMEM	Dulbecco's Modified Eagle Medium
$NaBH_4$	Sodium borohydride
MTT	3-(4,5-Dimethylthiazol-2-yl)-2,5-Diphenyltetrazolium Bromide
EDX	Energy-dispersive X-ray
CFU/mL	Colony forming unit per mL
LB	Luria broth
SCB	Sodium cacodylate

References

1. Hou, S.S.; Hasnat, M.; Chen, Z.W.; Liu, Y.N.; Baig, M.; Liu, F.H.; Chen, Z.L. Application Perspectives of Nanomedicine in Cancer Treatment. *Front. Pharmacol.* **2022**, *13*, 15. [CrossRef] [PubMed]
2. Smrke, A.; Anderson, P.M.; Gulia, A.; Gennatas, S.; Huang, P.H.; Jones, R.L. Future Directions in the Treatment of Osteosarcoma. *Cells* **2021**, *10*, 172. [CrossRef]
3. Ning, B.; Liu, Y.; Huang, T.; Wei, Y. Autophagy and its role in osteosarcoma. *Cancer Med.* **2023**, *12*, 5676–5687. [CrossRef]
4. Shen, F.; Fang, Y.; Wu, Y.; Zhou, M.; Shen, J.; Fan, X. Metal ions and nanometallic materials in antitumor immunity: Function, application, and perspective. *J. Nanobiotechnol.* **2023**, *21*, 20. [CrossRef]
5. Avnet, S.; Chano, T.; Massa, A.; Bonuccelli, G.; Lemma, S.; Falzetti, L.; Grisendi, G.; Dominici, M.; Baldini, N. Acid microenvironment promotes cell survival o human bone sarcoma through the activation of clAP proteins and NE-κB pathway. *Am. J. Cancer Res.* **2019**, *9*, 1127. [PubMed]
6. Chano, T.; Avnet, S.; Kusuzaki, K.; Bonuccelli, G.; Sonveaux, P.; Rotili, D.; Mai, A.; Baldini, N. Tumour-specific metabolic adaptation to acidosis is coupled to epigenetic stability in osteosarcoma cells. *Am. J. Cancer Res.* **2016**, *6*, 859–875.
7. Su, W.W.; Li, Y.Y.; Yang, G.; Zhao, Y.Y.; Zhou, X.H.; Liu, G.Y.; Huang, X.; Sohail, M.F.; Hussain, I.; Liu, Q.H.; et al. Nanotechnology-Driven Strategies in Osteosarcoma Advances in Treatment: Immunotherapy and Drug Delivery. *Int. J. Nanomed.* **2025**, *20*, 12913–12937. [CrossRef]
8. Wang, D.; Peng, Y.; Li, Y.Z.; Kpegah, J.; Chen, S.J. Multifunctional inorganic biomaterials: New weapons targeting osteosarcoma. *Front. Mol. Biosci.* **2023**, *9*, 18. [CrossRef]
9. Lim, Y.Y.; Zaidi, A.M.A.; Miskon, A. Combining Copper and Zinc into a Biosensor for Anti-Chemoresistance and Achieving Osteosarcoma Therapeutic Efficacy. *Molecules* **2023**, *28*, 2920. [CrossRef] [PubMed]
10. Jaishankar, M.; Tseten, T.; Anbalagan, N.; Mathew, B.B.; Beeregowda, K.N. Toxicity, mechanism and health effects of some heavy metals. *Interdiscip. Toxicol.* **2014**, *7*, 60–72. [CrossRef]
11. Jomova, K.; Makova, M.; Alomar, S.Y.; Alwasel, S.H.; Nepovimova, E.; Kuca, K.; Rhodes, C.J.; Valko, M. Essential metals in health and disease. *Chem. Biol. Interact.* **2022**, *367*, 110173. [CrossRef]
12. Djoko, K.Y.; Ong, C.L.Y.; Walker, M.J.; McEwan, A.G. The Role of Copper and Zinc Toxicity in Innate Immune Defense against Bacterial Pathogens. *J. Biol. Chem.* **2015**, *290*, 18954–18961. [CrossRef]
13. Paasche, G.; Ceschi, P.; Löbler, M.; Rösl, C.; Gomes, P.; Hahn, A.; Rohm, H.W.; Sternberg, K.; Lenarz, T.; Schmitz, K.P.; et al. Effects of Metal Ions on Fibroblasts and Spiral Ganglion Cells. *J. Neurosci. Res.* **2011**, *89*, 611–617. [CrossRef] [PubMed]
14. Bremner, I.; Beattie, J.H. Copper and zinc-metabolism in health and disease—Speciation and interactions. *Proc. Nutr. Soc.* **1995**, *54*, 489–499. [CrossRef] [PubMed]
15. Cheignon, C.; Tomas, M.; Bonnefont-Rousselot, D.; Faller, P.; Hureau, C.; Collin, F. Oxidative stress and the amyloid beta peptide in Alzheimer's disease. *Redox Biol.* **2018**, *14*, 450–464. [CrossRef]
16. Qin, S.; Hu, Y.F.; Luo, H.S.; Chu, W.; Deng, R.C.; Ma, J.L. Metal ions and nanomaterials for targeted bone cancer immunotherapy. *Front. Immunol.* **2025**, *16*, 15. [CrossRef]
17. Sidhu, A.K.; Verma, N.; Kaushal, P. Role of Biogenic Capping Agents in the Synthesis of Metallic Nanoparticles and Evaluation of Their Therapeutic Potential. *Front. Nanotechnol.* **2022**, *3*, 17. [CrossRef]
18. Bassan, G.A.; Marchesan, S. Peptide-Based Materials That Exploit Metal Coordination. *Int. J. Mol. Sci.* **2023**, *24*, 456. [CrossRef]
19. Cao, M.W.; Xing, R.R.; Chang, R.; Wang, Y.; Yan, X.H. Peptide-coordination self-assembly for the precise design of theranostic nanodrugs. *Coord. Chem. Rev.* **2019**, *397*, 14–27. [CrossRef]
20. Zechel, S.; Hager, M.D.; Priemel, T.; Harrington, M.J. Healing through histidine: Bioinspired pathways to self-healing polymers via imidazole-metal coordination. *Biomimetics* **2019**, *4*, 20. [CrossRef]
21. Chen, Y.; Tao, K.; Ji, W.; Kumar, V.B.; Rencus-Lazar, S.; Gazit, E. Histidine as a key modulator of molecular self-assembly: Peptide-based supramolecular materials inspired by biological systems. *Mater. Today* **2022**, *60*, 106–127. [CrossRef]

22. Uthaman, S.; Huh, K.M.; Park, I.K. Tumor microenvironment-responsive nanoparticles for cancer theragnostic applications. *Biomater. Res.* **2018**, *22*, 22. [CrossRef]
23. Glymenaki, E.; Kandyli, M.; Apostolidou, C.P.; Kokotidou, C.; Charalambidis, G.; Nikoloudakis, E.; Panagiotakis, S.; Koutserinaki, E.; Klontza, V.; Michail, P.; et al. Design and Synthesis of Porphyrin-Nitrilotriacetic Acid Dyads with Potential Applications in Peptide Labeling through Metallochelate Coupling. *ACS Omega* **2022**, *7*, 1803–1818. [CrossRef]
24. Li, S.K.; van Hest, J.C.M.; Xing, R.R.; Yan, X.H. Peptide self-assembly meets photodynamic therapy: From molecular design to antitumor applications. *Chem. Commun.* **2025**, *61*, 13841–13851. [CrossRef] [PubMed]
25. Falanga, A.; Nigro, E.; De Biasi, M.G.; Daniele, A.; Morelli, G.; Galdiero, S.; Scudiero, O. Cyclic Peptides as Novel Therapeutic Microbicides: Engineering of Human Defensin Mimetics. *Molecules* **2017**, *22*, 1217. [CrossRef]
26. Zhao, K.L.; Xing, R.R.; Yan, X.H. Cyclic dipeptides: Biological activities and self-assembled materials. *Pept. Sci.* **2021**, *113*, 13. [CrossRef]
27. Chen, Y.; Orr, A.A.; Tao, K.; Wang, Z.B.; Ruggiero, A.; Shimon, L.J.W.; Schnaider, L.; Goodall, A.; Rencus-Lazar, S.; Gilead, S.; et al. High-Efficiency Fluorescence through Bioinspired Supramolecular Self-Assembly. *ACS Nano* **2020**, *14*, 2798–2807. [CrossRef] [PubMed]
28. Vlachou, A.; Kumar, V.B.; Tiwari, O.S.; Rencus-Lazar, S.; Chen, Y.; Ozguney, B.; Gazit, E.; Tamamis, P. Co-Assembly of Cancer Drugs with Cyclo-HH Peptides: Insights from Simulations and Experiments. *ACS Appl. Bio Mater.* **2024**, *7*, 2309–2324. [CrossRef]
29. Vlachou, A.; Tiwari, O.S.; Chibh, S.; Remmert, J.R.; Gazit, E.; Tamamis, P. Minimalistic Peptide Nanocarriers for Multiple Cancer Drugs. *ACS Appl. Bio Mater.* **2025**, *8*, 9093–9108. [CrossRef]
30. McCleland, K.; Milne, P.J.; Lucieto, F.R.; Frost, C.; Brauns, S.C.; Van De Venter, M.; Du Plessis, J.; Dyason, K. An investigation into the biological activity of the selected histidine-containing diketopiperazines cyclo(His-Phe) and cyclo(His-Tyr). *J. Pharm. Pharmacol.* **2010**, *56*, 1143–1153. [CrossRef]
31. Rohani, N.; Hao, L.L.; Alexis, M.S.; Joughin, B.A.; Krismer, K.; Moufarrej, M.N.; Soltis, A.R.; Lauffenburger, D.A.; Yaffe, M.B.; Burge, C.B.; et al. Acidification of Tumor at Stromal Boundaries Drives Transcriptome Alterations Associated with Aggressive Phenotypes. *Cancer Res.* **2019**, *79*, 1952–1966. [CrossRef] [PubMed]
32. Sahariah, P.; Kontogianni, G.I.; Scoulica, E.; Sigurjonsson, O.E.; Chatzinikolaidou, M. Structure-activity relationship for antibacterial chitosan carrying cationic and hydrophobic moieties. *Carbohydr. Polym.* **2023**, *312*, 15. [CrossRef]
33. Fukui, H.; Iwahashi, H.; Nishio, K.; Hagihara, Y.; Yoshida, Y.; Horie, M. Ascorbic acid prevents zinc oxide nanoparticle-induced intracellular oxidative stress and inflammatory responses. *Toxicol. Ind. Health* **2017**, *33*, 687–695. [CrossRef]
34. Knight, A.S.; Larsson, J.; Ren, J.M.; Zerdan, R.B.; Seguin, S.; Vrahas, R.; Liu, J.; Ren, G.; Hawker, C.J. Control of Amphiphile Self-Assembly via Bioinspired Metal Ion Coordination. *J. Am. Chem. Soc.* **2018**, *140*, 1409–1414. [CrossRef]
35. Gunawan, L.; Johari, G.P. Specific Heat, Melting, Crystallization, and Oxidation of Zinc Nanoparticles and Their Transmission Electron Microscopy Studies. *J. Phys. Chem. C* **2008**, *112*, 20159–20166. [CrossRef]
36. Wang, Z.Y.; von dem Bussche, A.; Kabadi, P.K.; Kane, A.B.; Hurt, R.H. Biological and Environmental Transformations of Copper-Based Nanomaterials. *ACS Nano* **2013**, *7*, 8715–8727. [CrossRef] [PubMed]
37. Seo, J.; Hoffmann, W.; Warnke, S.; Huang, X.; Gewinner, S.; Schöllkopf, W.; Bowers, M.T.; Von Helden, G.; Pagel, K. An infrared spectroscopy approach to follow β-sheet formation in peptide amyloid assemblies. *Nat. Chem.* **2017**, *9*, 39–44. [CrossRef] [PubMed]
38. Fadlelmoula, A.; Pinho, D.; Carvalho, V.H.; Catarino, S.O.; Minas, G. Fourier Transform Infrared (FTIR) Spectroscopy to Analyse Human Blood over the Last 20 Years: A Review towards Lab-on-a-Chip Devices. *Micromachines* **2022**, *13*, 187. [CrossRef]
39. Yang, H.; Pritzker, M.; Fung, S.Y.; Sheng, Y.; Wang, W.; Chen, P. Anion effect on the nanostructure of a metal Ion binding self-assembling peptide. *Langmuir* **2006**, *22*, 8553–8562. [CrossRef]
40. Celik, S.; Ozel, A.E.; Kecel, S.; Akyuz, S. Structural and IR and Raman spectral analysis of cyclo(His-Phe) dipeptide. *Vib. Spectrosc.* **2012**, *61*, 54–65. [CrossRef]
41. Manchineella, S.; Govindaraju, T. Molecular Self-Assembly of Cyclic Dipeptide Derivatives and Their Applications. *ChemPlusChem* **2017**, *82*, 88–106. [CrossRef] [PubMed]
42. Reddy, P.R.; Radhika, M.; Manjula, P. Synthesis and characterization of mixed ligand complexes of Zn(II) and Co(II) with amino acids: Relevance to zinc binding sites in zinc fingers. *J. Chem. Sci.* **2005**, *117*, 239–246. [CrossRef]
43. Faheem, M.; Siddiqi, H.M.; Habib, A.; Shahid, M.; Afzal, A. $ZnO/Zn(OH)_2$ nanoparticles and self-cleaning coatings for the photocatalytic degradation of organic pollutants. *Front. Environ. Sci.* **2022**, *10*, 9. [CrossRef]
44. Gustiananda, M.; Haris, P.I.; Milburn, P.J.; Gready, J.E. Copper-induced conformational change in a marsupial prion protein repeat peptide probed using FTIR spectroscopy. *FEBS Lett.* **2002**, *512*, 38–42. [CrossRef]
45. Mendes, C.R.; Dilarri, G.; Forsan, C.F.; Sapata, V.D.R.; Lopes, P.R.M.; de Moraes, P.B.; Montagnolli, R.N.; Ferreira, H.; Bidoia, E.D. Antibacterial action and target mechanisms of zinc oxide nanoparticles against bacterial pathogens. *Sci. Rep.* **2022**, *12*, 10. [CrossRef]
46. Shaffner, T.J.; Vanveld, R.D. Charging effects in scanning electron microscope. *J. Phys. E Sci. Instrum.* **1971**, *4*, 633–637. [CrossRef]

47. Sreevalsa, V.G.; Jeeju, P.P.; Augustine, M.S.; Anilkumar, K.M.; Jayalekshmi, S. L-Histidine-modified biocompatible zinc oxide nanocrystals. *J. Exp. Nanosci.* **2013**, *8*, 937–946. [CrossRef]
48. Chohan, Z.H.; Arif, M.; Akhtar, M.A.; Supuran, C.T. Metal-based antibacterial and antifungal agents: Synthesis, characterization, and in vitro biological evaluation of Co(II), Cu(II), Ni(II), and Zn(II) complexes with amino acid-derived compounds. *Bioinorg. Chem. Appl.* **2006**, *2006*, 83131. [CrossRef]
49. Dutour, A.; Pasello, M.; Farrow, L.; Amer, M.H.; Entz-Werle, N.; Nathrath, M.; Scotlandi, K.; Mittnacht, S.; Gomez-Mascard, A. Microenvironment matters: Insights from the FOSTER consortium on microenvironment-driven approaches to osteosarcoma therapy. *Cancer Metastasis Rev.* **2025**, *44*, 22. [CrossRef] [PubMed]
50. Kim, H.; Taslakjian, B.; Kim, S.; Tirrell, M.V.; Guler, M.O. Therapeutic Peptides, Proteins and their Nanostructures for Drug Delivery and Precision Medicine. *Chembiochem* **2024**, *25*, 21. [CrossRef] [PubMed]
51. Kortam, S.; Lu, Z.F.; Zreiqat, H. Recent advances in drug delivery systems for osteosarcoma therapy and bone regeneration. *Commun. Mater.* **2024**, *5*, 20. [CrossRef]
52. Shi, P.; Cheng, Z.; Zhao, K.; Chen, Y.; Zhang, A.; Gan, W.; Zhang, Y. Active targeting schemes for nano-drug delivery systems in osteosarcoma therapeutics. *J. Nanobiotechnol.* **2023**, *21*, 103. [CrossRef]
53. Ai, J.W.; Liao, W.; Ren, Z.L. Enhanced anticancer effect of copper-loaded chitosan nanoparticles against osteosarcoma. *RSC Adv.* **2017**, *7*, 15971–15977. [CrossRef]
54. Magrì, A.; Marrone, A.; Tolbatov, I.; Tabbì, G.; Chiaverini, L.; Attanasio, F.; Marzo, T.; Naletova, I.; La Mendola, D. Copper(II) binding properties and anticancer activity of peptide fragments from a β-strand region of angiogenin protein. *Inorg. Chim. Acta* **2025**, *582*, 122680. [CrossRef]
55. Gahan, L.R.; Cusack, R.M. Metal complexes of synthetic cyclic peptides. *Polyhedron* **2018**, *153*, 1–23. [CrossRef]
56. Bojarska, J.; Mieczkowski, A.; Ziora, Z.M.; Skwarczynski, M.; Toth, I.; Shalash, A.O.; Parang, K.; El-Mowafi, S.A.; Mohammed, E.H.M.; Elnagdy, S.; et al. Cyclic Dipeptides: The Biological and Structural Landscape with Special Focus on the Anti-Cancer Proline-Based Scaffold. *Biomolecules* **2021**, *11*, 1515. [CrossRef]
57. Siddiqi, K.S.; ur Rahman, A.; Tajuddin; Husen, A. Properties of Zinc Oxide Nanoparticles and Their Activity Against Microbes. *Nanoscale Res. Lett.* **2018**, *13*, 141. [CrossRef]
58. Kordi, M.; Borzouyi, Z.; Chitsaz, S.; Asmaei, M.H.; Salami, R.; Tabarzad, M. Antimicrobial peptides with anticancer activity: Today status, trends and their computational design. *Arch. Biochem. Biophys.* **2023**, *733*, 109484. [CrossRef]
59. Tornesello, A.L.; Borrelli, A.; Buonaguro, L.; Buonaguro, F.M.; Tornesello, M.L. Antimicrobial Peptides as Anticancer Agents: Functional Properties and Biological Activities. *Molecules* **2020**, *25*, 2850. [CrossRef] [PubMed]
60. Xiong, L.; Tong, Z.-H.; Chen, J.-J.; Li, L.-L.; Yu, H.-Q. Morphology-dependent antimicrobial activity of Cu/CuxO nanoparticles. *Ecotoxicology* **2015**, *10*, 2067–2072.
61. Ren, G.G.; Hu, D.W.; Cheng, E.W.C.; Vargas-Reus, M.A.; Reip, P.; Allaker, R.P. Characterisation of copper oxide nanoparticles for antimicrobial applications. *Int. J. Antimicrob. Agents* **2009**, *33*, 587–590. [CrossRef]
62. Reed, R.B.; Ladner, D.A.; Higgins, C.P.; Westerhoff, P.; Ranville, J.F. Solubility of nano-zinc oxide in environmentally and biologically important matrices. *Environ. Toxicol. Chem.* **2012**, *31*, 93–99. [CrossRef] [PubMed]
63. Guo, Z.S.; Chen, H.H.; Hu, R.L.; Wang, J.W.; Wu, M.; Wu, Y.H.; Qiang, T.H.; Mou, H.; Du, X.G.; Gao, F.; et al. Study of antibacterial activity of copper zinc nanocomposites and disruption of bacterial cytoplasmic membrane. *Sci. Rep.* **2025**, *15*, 16. [CrossRef] [PubMed]
64. Chen, Q.; Espey, M.G.; Krishna, M.C.; Mitchell, J.B.; Corpe, C.P.; Buettner, G.R.; Shacter, E.; Levine, M. Pharmacologic ascorbic acid concentrations selectively kill cancer cells: Action as a pro-drug to deliver hydrogen peroxide to tissues. *Proc. Natl. Acad. Sci. USA* **2005**, *102*, 13604–13609. [CrossRef]
65. Arunsi, U.O.; Olugbami, J.O.; Oyelere, A.K. Anticancer Effects of Ascorbic Acid: Not All Sides Fit All. *Cancers* **2025**, *17*, 2877. [CrossRef] [PubMed]
66. Hadi, S.M.; Ullah, M.F.; Shamim, U.; Bhatt, S.H.; Azmi, A.S. Catalytic Therapy of Cancer by Ascorbic Acid Involves Redox Cycling of Exogenous/Endogenous Copper Ions and Generation of Reactive Oxygen Species. *Chemotherapy* **2010**, *56*, 280–284. [CrossRef]